

1 1.5em 0pt

2 Integrated Simulation of Three-Dimensional Hydraulic  
3 Fracture Propagation and Lagrangian Proppant  
4 Transport in Multilayered Reservoirs

5 **Shaowen Mao<sup>a,b,\*</sup>, Kan Wu<sup>b</sup>, George Moridis<sup>b,c</sup>**

6 <sup>a</sup>Los Alamos National Laboratory

7 <sup>b</sup>Texas A&M University

8 <sup>c</sup>Lawrence Berkeley National Laboratory

9 \*Corresponding author; email: shaowen.mao@tamu.edu

10 **Abstract**

11 The numerical simulation of hydraulic fractures is a critical yet challenging computational problem due to  
12 its multi-physics nature. This paper develops an integrated hydraulic fracturing simulator by coupling a  
13 planar three-dimensional (PL3D) fracture propagation model with an efficient Eulerian-Lagrangian (E-L)  
14 proppant transport model. The fracture propagation model uses the finite volume method (FVM) and  
15 displacement discontinuity method (DDM) to solve the fluid flow and rock deformation, respectively. For  
16 proppant transport, we develop a pseudo-3D multiphase particle-in-cell (P3D MP-PIC) model, in which the  
17 fluid flow is addressed by FVM as a continuum, but the particles are tracked in a Lagrangian fashion as  
18 discrete phases. In contrast to Eulerian-Eulerian (E-E) proppant transport models, the P3D MP-PIC can  
19 efficiently deal with multi-modal particle simulations (i.e., particles of different sizes or materials) and avoid  
20 the problem of numerical diffusion. The fracture propagation and proppant transport models are validated  
21 by analytical solutions and laboratory experiments. We adopt a one-way coupling strategy to consider the  
22 effect of complex fracture propagation and fluid leak-off on slurry transport, in which the dynamic fracture  
23 geometry and fluid leak-off is first computed via the fracture propagation model, followed by the fully coupled  
24 fluid-particle simulation using the P3D MP-PIC. The integrated model can simulate the fracturing treatments  
25 in multilayered reservoirs with varying confining stresses at an industrial field scale. The simulation results  
26 can improve the prediction of effective/propped fracture geometries and better the fracturing designs.

## 27 1 Introduction

28 Hydraulic fractures are tensile fractures that propagate in solid media under pre-existing compressive stress  
29 due to high-pressure fluid injection. Hydraulic fractures widely occur in both natural geological processes  
30 and subsurface engineering applications. The natural occurrence includes vertical dikes bringing magma  
31 from the underground to the earth's surface (Spence et al. 1987; Roper and Lister 2005, 2007), horizontal  
32 sills diverting magma from dikes (Pollard and Hozlhausen 1979; Bunger and Cruden 2011), and cracks  
33 propagating at glacier beds (Tsai and Rice 2010). The engineering applications involve the stimulation of  
34 hydrocarbon and geothermal reservoirs (Economides and Nolte 1989; Zimmerman et al. 2011; Ghassemi  
35 2012; McClure and Horne 2014; Tang and Wu 2018; Dontsov and Suarez 2021), preconditioning in rock  
36 mining (van As and Jeffrey 2002; Jeffrey et al. 2013), remediation of contaminated soils (Frank and Barkley  
37 1995; Murdoch 2002), disposal of nuclear wastes (Salimzadeh et al. 2020; Xu et al. 2020), and measurement  
38 of in-situ stresses (Zoback and Haimson 1982; Detournay et al. 1989; Kim et al. 2017).

39 The numerical simulation of hydraulic fracture propagation is a challenging computational problem be-  
40 cause it involves multiple physical processes, such as the mechanical deformation of the rock medium, fluid  
41 flow in the fracture, and fluid leak-off into the host rock. Significant research progress has been made over  
42 the past decades in modeling fluid-driven fractures (Khristianovic and Zheltov 1955; Perkins and Kern 1961;  
43 Geertsma and De Klerk 1969; Nordgren 1972; Mendelsohn 1984; Bunger et al. 2005; Adachi et al. 2007;  
44 Weng et al. 2011; Donstov and Peirce 2015, 2017; Lecampion and Desroches 2015; Wu and Olson 2015;  
45 Donstov 2016; Detournay 2004, 2016; Chen et al. 2020; Li and Zhang 2021). However, there are still some  
46 issues warranting further investigation, of which the proppant transport is of great significance. Proppant  
47 represents a granular material that prevents complete closure of the hydraulic fracture after treatments,  
48 generating a highly conductive pathway. Accurate modeling of proppant settling and migration within  
49 the fracture is critical to predicting the effective/propped fracture geometry and optimizing the fracturing  
50 designs.

51 The numerical models to simulate the fluid-particle system are within the Eulerian-Eulerian (E-E) and  
52 Eulerian-Lagrangian (E-L) frameworks. The E-E framework treats both the fluid and particles as continua,  
53 while the E-L framework treats the fluid as a continuum but the particles as discrete phases. E-E models,  
54 such as the concentration model (Sharma and Gadde 2005; Gu and Mohanty 2014; Dontsov and Peirce 2014;  
55 Roostaei et al. 2018; Chen et al. 2022; Huang et al. 2022) and two-fluid model (Mobbs and Hammond 2001;  
56 Boronin and Osiptsov 2014), are widely used in commercial software because of the computational efficiency  
57 and flexibility to be coupled with other subsurface processes. However, it is difficult for the E-E methods to  
58 consider multi-modal simulations (i.e., particles of different sizes or materials). In contrast, the E-L models

59 can easily deal with multi-modal simulations and avoid the problem of numerical diffusion by tracking the  
60 particles in a Lagrangian fashion (Andrews and Rourke 1996; Patankar and Joseph 2001). Therefore, the  
61 E-L models have become increasingly popular in simulating slurry flow in hydraulic fracturing, where multi-  
62 modal proppant is typically loaded during treatments (Patankar and Joseph 2001; Tsai et al. 2012; Zeng et  
63 al. 2016, 2019, 2022; Kou et al. 2018, 2019; Wu and Sharma 2019; Zhang et al. 2020 a, b; Suri et al. 2020;  
64 Mao et al. 2021 a, b and 2022; Zhang et al. 2022).

65 The E-L models for proppant transport simulation can be classified into micro-, meso-, and macro-scale  
66 approaches based on the characteristic length (Table 1). The micro-scale models, such as the resolved  
67 computational fluid dynamics-discrete element method (resolved CFD-DEM), resolve the fluid field around  
68 each particle, focusing on particle-scale physics. The meso-scale models, including the unresolved CFD-DEM,  
69 the dense discrete phase model (DDPM), and the multiphase particle-in-cell (MP-PIC) method, assemble  
70 particles into computational parcels (pseudo particles) by upscaling techniques to reduce the number of  
71 particles involved in the calculation, thus speeding up the simulation. The macro-scale models (e.g., pseudo-  
72 3D (P3D) MP-PIC) have the best computational efficiency to perform industrial field-scale simulations.  
73 Note that each micro-, meso- and macro-scale model has its values and roles in characterizing the proppant  
74 transport behaviors at a corresponding scale. The approach of different scales is linked with each other to  
75 form a comprehensive multi-scale modeling framework.

Literature	Model	Dimension	Scale	Fracture Geometry
Pola et al. 2017; Zeng et al. 2021, 2022	Resolved CFD-DEM	3D	Micro-scale (~ 0.01 m)	Static fracture
Zeng et al. 2016, 2021; Kou et al. 2018, 2019; Baldini et al. 2018	Unresolved CFD-DEM	3D	Meso-scale (~ 1 m)	Static fracture
Suri et al. 2020	Unresolved CFD-DEM	3D	Meso-scale (~ 1 m)	Dynamic fracture propagation (XFEM)
Tong and Mohanty 2016; Hu et al. 2018; Wen et al. 2020	DDPM	3D	Meso-scale (~ 1 m)	Static fracture
Patankar and Joseph 2001; Tsai et al. 2013; Siddhamshetty et al. 2020; Mao et al. 2021 a, b; Zhang et al. 2021 a, b	MP-PIC	3D	Meso-scale (~ 1 m)	Static fracture
Zeng et al. 2019	MP-PIC	Pseudo 3D	Macro-scale (~ 100 m)	Dynamic analytical (PKN) fracture
Mao et al. 2022	MP-PIC	Pseudo 3D	Macro-scale (~ 100 m)	Dynamic analytical (KGD) fracture

**Table 1:** Literature review of Eulerian-Lagrangian (E-L) models for proppant transport simulation.

This work mainly focuses on the integrated simulation of fracture propagation and proppant transport at the macro scale. There have been numerous contributions to developing macro-scale integrated hydraulic fracturing simulators (Dontsov and Peirce 2015; Shiozawa and McClure 2016; Kumar and Ghassemi 2021; Chen et al. 2022; Zhang et al. 2022; Luo et al. 2023). However, most existing simulators adopt E-E models for proppant transport simulation. The coupling of fracture propagation with E-L proppant transport models remains particularly challenging. As illustrated in Table 1, most studies assume static fracture geometries when applying E-L models in proppant transport simulation. Zeng et al. 2019 and Mao et al. 2022 proposed integrated models by coupling a P3D MP-PIC method with 2D analytical fracture propagation models (PKN and KGD), considering the effect of fracture propagation and fluid leak-off on proppant transport. However, these models assume oversimplified fracture geometries and only deal with single-layer reservoirs. Suri et al. 2020 proposed an integrated numerical approach in which the proppant transport is simulated by the unresolved CFD-DEM, and the fracture propagation is modeled by the cohesive-based extended finite element method (XFEM). Suri's model generates more realistic fracture geometries, but it is difficult to perform industrial field-scale simulations due to the high computational cost of unresolved CFD-DEM.

To overcome the above limitations, we have developed an integrated hydraulic fracturing simulator by coupling a planar 3D (PL3D) fracture propagation model with an efficient E-L proppant transport model. The fracture propagation model uses the finite volume method (FVM) and displacement discontinuity method (DDM) to solve the fluid flow and rock deformation, respectively. The proppant transport is modeled by the P3D MP-PIC method. The fracture propagation and proppant transport are one-way coupled. To the best of our knowledge, this is the first macro-scale hydraulic fracturing simulator to couple a PL3D fracture propagation model with an E-L proppant transport model. The current model can simulate complex fracture propagation and particle transport behaviors in multilayer reservoirs at the industrial field scale.

This paper is organized as follows. Section 2 describes the mathematical formulation for the hydraulic fracture propagation and proppant transport models, followed by the discretization of the governing equations in Section 3. Section 4 presents a numerical solution strategy for solving the coupled system. Section 5 validates the fracture propagation and proppant transport models by analytical solutions and laboratory experiments. Section 6 performs the field-scale application to demonstrate the model's functionality, and Section 7 concludes this paper.

## 2 Mathematical Formulation

This study focuses on the integrated numerical simulation of hydraulic fracturing treatments, including the fracture propagation and proppant transport processes (Fig.1). The fracture propagation is modeled by a

107 high-fidelity PL3D fracture propagation model, and the proppant transport is simulated via an efficient P3D  
 108 MP-PIC model. This section provides a detailed mathematical description of these models.

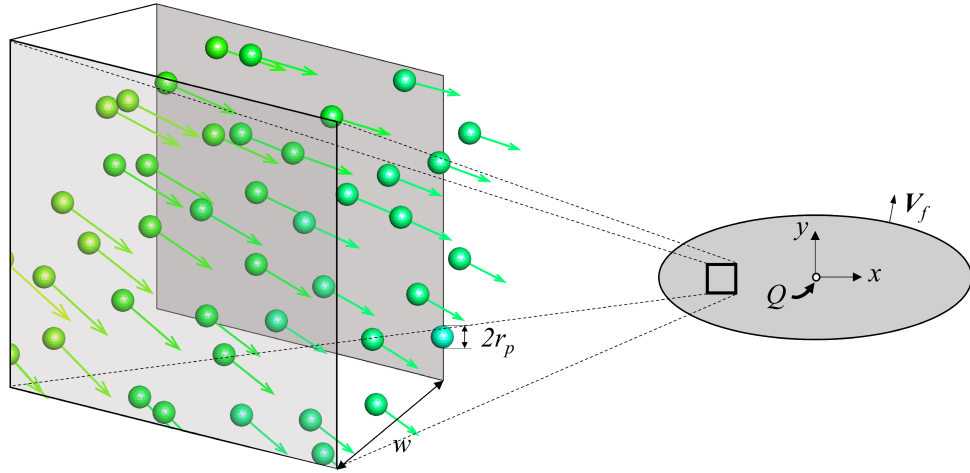


**Figure 1:** Schematics of the hydraulic fracturing process, including the fracture propagation (right) and proppant transport (left).  $w$  is the fracture width.  $r_p$  is the particle radius.  $Q$  is the injection rate.  $V_f$  is the fracture front velocity.

## 109 2.1 Assumptions

110 A series of assumptions are introduced to make the problem more tractable.

- 111 • The hydraulic fracture grows in mode I (pure tension) in a homogeneous and elastic rock medium with  
 112 uniform values of rock toughness  $K_{Ic}$ , Young's modulus  $E$ , and Poisson's ratio  $\nu$ ;
- 113 • The fracturing fluid is incompressible and Newtonian, and the fluid gravity is neglected;
- 114 • The fluid leak-off can be modeled using Carter's theory (1957) with a constant leak-off coefficient  $C_L$ ;
- 115 • The fracture front coincides with the fluid front due to the high confining stress in reservoirs (Garagash  
 116 and Detournay, 2000);
- 117 • The fluid flow and particle transport in the fracture width direction are neglected because of the large  
 118 aspect ratio of hydraulic fracture geometries ( $\sim 10^5$ );
- 119 • The proppant transport has a negligible effect on fracture propagation due to the huge amount of pad  
 120 fluid injection.

## 121 2.2 Hydraulic Fracture Propagation

122 The formulation of the fracture evolution problem includes two fundamental equations (elasticity equation  
 123 and lubrication equation) and the initial and boundary conditions. Four combinations of material parameters  
 124 are defined in scaled form to simplify the equations.

$$E' = \frac{E}{1-v^2}, C' = 2C_L, \mu' = 12\mu, K' = 4 \left( \frac{2}{\pi} \right)^{1/2} K_{Ic}, \quad (1)$$

125 where  $E'$  is the plane-strain modulus.  $C'$ ,  $\mu'$ , and  $K'$  are the alternative leak-off coefficient, viscosity,  
126 and toughness, respectively.

### 127 2.2.1 Elasticity

128 The non-local elasticity equation is expressed as a hypersingular integral equation, relating the fracture  
129 width  $w$  to the internal fluid pressure  $p$  as (Crouch et al. 1983; Hills et al. 1996; Detournay 2016)

$$p(\mathbf{x}, t) - \sigma_0(\mathbf{x}) = -\frac{E'}{8\pi} \int_{A(t)} \frac{w(\mathbf{x}', t)}{|\mathbf{x} - \mathbf{x}'|} dA(\mathbf{x}'), \quad (2)$$

130 where  $\mathbf{x}$  and  $t$  are the position vector and injection time, respectively.  $A$  is the fracture footprint.  $\sigma_0$  is  
131 the minimum in-situ compressive principal stress.

132 **2.2.2 Lubrication** The nonlinear lubrication equation governs the mass balance of an incompressible  
133 Newtonian fluid inside the fracture and can be written as

$$\frac{\partial w}{\partial t} + \frac{C'}{\sqrt{t - \tau(\mathbf{x})}} = \frac{1}{\mu'} \nabla \cdot (w^3 \nabla p) + Q(t) \delta(\mathbf{x}), \quad (3)$$

134 where the  $C'/\sqrt{t - \tau(\mathbf{x})}$  term represents the fluid leak-off into the host rock via Carter's model (Carter  
135 1957).  $\tau(\mathbf{x})$  is the time at which the leak-off begins at a point  $\mathbf{x}$  on the fracture surface. The boundary  
136 condition at the injection point is incorporated via the singular term  $Q(t)\delta(\mathbf{x})$ .

### 137 2.2.3 Boundary and Initial Conditions

138 A no-flow condition and zero-width condition are applied on the moving fracture front.

$$\mathbf{q}(\mathbf{x}_{\text{front}}, t) = 0, w(\mathbf{x}_{\text{front}}, t) = 0 \quad (4)$$

139 Here,  $\mathbf{q} = -w^3/\mu' \nabla p$  based on Poiseuille's law for the fluid flux.

140 The fracture width in the tip region follows the classical result of linear elastic fracture mechanics (LEFM).

$$\lim_{s \rightarrow 0} w \simeq \frac{K'}{E'} s^{1/2}, \quad (5)$$

141 where  $s$  is the inward distance from the fracture tip.

142 The initial condition expresses a zero-fracture width field as

$$w(\mathbf{x}, 0) = 0, \forall \mathbf{x} \in A \quad (6)$$

143      **2.3 Proppant Transport**

144      The proppant transport is simulated by an efficient P3D MP-PIC method, which adopts an Eulerian  
 145      approach for the fluid phase but a Lagrangian description for the particle phases. The governing equations  
 146      for the E-L formulation are shown as follows.

147      **2.3.1 Fluid Phase**

148      We use equations for the average properties of the fluid phase (Tsuo and Gidaspow 1990; Patankar and  
 149      Joseph 2001; Crowe et al. 2011; Zeng et al. 2019). The continuity equation is

$$\frac{\partial(\theta_f w)}{\partial t} + \nabla \cdot (\theta_f \mathbf{u}_f w) + s_l - Q(t)\delta(\mathbf{x}) = 0, \quad (7)$$

150      where  $\theta_f$  is the fluid volume fraction.  $\mathbf{u}_f$  is the fluid velocity. By incorporating the fracture width  
 151       $w(\mathbf{x}, t)$  and fluid leak-off rate  $s_l(\mathbf{x}, t)$  into Eq. 7, the model can consider the effect of fracture propagation  
 152      and fluid leak-off processes on the proppant transport. The singular term  $Q(t)\delta(\mathbf{x})$  accounts for the boundary  
 153      condition at the injection point.

154      The momentum equation is

$$\frac{1}{w} \frac{\partial(\theta_f w \mathbf{u}_f)}{\partial t} + \frac{1}{w} \nabla \cdot (w \theta_f \mathbf{u}_f \mathbf{u}_f - w \mu_f \nabla \mathbf{u}_f) = -\frac{1}{\rho_f} \nabla p - \frac{1}{\rho_f} \mathbf{F} - \mathbf{F}_w, \quad (8)$$

155      where  $\mu_f$  is the slurry viscosity.  $\mathbf{F}$  is the rate of interphase moment transfer per unit volume, and the  
 156      detailed expression will be presented later in this section. The body force due to fluid gravity is balanced  
 157      by the hydrostatic pressure and does not appear explicitly in the equation. A wall friction term  $\mathbf{F}_w$  is  
 158      incorporated to account for the fluid flow resistance caused by fracture surfaces. Based on the plane Poiseuille  
 159      flow (Munson et al. 2006),  $\mathbf{F}_w$  is calculated by

$$\mathbf{F}_w = -\frac{12\mu_f}{\rho_f w^2} \mathbf{u}_f. \quad (9)$$

160      The slurry viscosity is calculated as (Barree and Conway 1994)

$$\mu_f = \mu_o \left(1 - \frac{\theta_p}{\theta_{cp}}\right)^{-1.82}, \quad (10)$$

161      where  $\theta_p$  is the particle volume fraction.  $\theta_p^c$  is the close-packing particle volume fraction.  $\mu_o$  is the  
 162      dynamic viscosity of the clean fluid.

163      **2.3.1 Particulate Phase**

164      The evolution of particle phase is governed by a Liouville equation for the particle distribution function  
 165       $\phi(\mathbf{x}_p, \mathbf{u}_p, \rho_p, V_p, t)$  (Snider 2001)

$$\frac{\partial \phi}{\partial t} + \nabla \cdot (\phi \mathbf{u}_p) + \nabla_{u_p} \cdot (\phi \mathbf{A}) = 0, \quad (11)$$

where  $\mathbf{x}_p$  is the particle position.  $\mathbf{u}_p$  is the particle velocity.  $\rho_p$  is the particle density.  $V_p$  is the particle volume.  $\nabla_{u_p}$  is the divergence operator with respect to particle velocity.  $\mathbf{A}$  is the particle acceleration expressed as

$$\mathbf{A} = \frac{d\mathbf{u}_p}{dt} = D_p (\mathbf{u}_f - \mathbf{u}_p) - \frac{1}{\rho_p} \nabla p + \left(1 - \frac{\rho_f}{\rho_p}\right) \mathbf{g} - \frac{1}{\theta_p \rho_p} \nabla \tau + \frac{\langle \mathbf{u}_p \rangle - \mathbf{u}_p}{2\tau_D}, \quad (12)$$

where the right-hand side terms represent the effect of fluid-particle drag, dynamic pressure gradient, net buoyant force, particle stress, and particle collision damping, respectively. Here,  $\mathbf{g}$  is the drag coefficient.  $\theta_p$  is the gravitational acceleration.  $D_p$  is the particle volume fraction.  $\tau$  is the interparticle stress.  $\langle \mathbf{u}_p \rangle$  is the mass-averaged particle velocity.  $\tau_D$  is the collision damping time. Note that the collision damping only takes effect in the close packing region (proppant bed), and the detailed expressions of  $\langle \mathbf{u}_p \rangle$  and  $\tau_D$  are given in Rourke and Snider (2010) and Zeng et al. (2019).

The fluid-particle drag coefficient  $D_p$  is calculated as (Gidaspow et al. 1994)

$$D_p = C_d \frac{3}{8} \frac{\rho_f |\mathbf{u}_f - \mathbf{u}_p|}{r_p}, \quad (13)$$

where

$$C_d = \begin{cases} \frac{24}{Re_p} \theta_f^{-2.65} (1 + 0.5 Re_p^{0.687}), & Re_p < 1000 \\ 0.44 \theta_f^{-2.65}, & Re_p \geq 1000 \end{cases}. \quad (14)$$

Here,  $C_d$  is the dimensionless drag coefficient (Wen et al. 1966).  $r_p$  is the particle radius.  $Re_p$  is the particle Reynolds number calculated by

$$Re_p = \frac{2\rho_f |\mathbf{u}_f - \mathbf{u}_p| r}{\mu_f}. \quad (15)$$

The interparticle stress  $\tau$  is modeled by (Harris and Crighton. 1994, Snider 2001)

$$\tau = \frac{P_s \theta_p^\beta}{\max [\theta_{cp} - \theta_p, \varepsilon (1 - \theta_p)]}, \quad (16)$$

where  $P_s$  and  $\beta$  are model constants set as 4 Pa and 2, respectively, based on the recommendation of Snider et al. (2001).  $\varepsilon$  is a small number on the order of  $10^{-7}$ , removing the singularity at close pack condition. The particle volume fraction  $\theta_p$  is defined by

$$\theta_p = \iiint \phi V_p dV_p d\rho_p d\mathbf{u}_p. \quad (17)$$

183 The fluid volume fraction  $\theta_f$  is then calculated by

$$\theta_f = 1 - \theta_p \quad (18)$$

184 The fluid and particle phases are coupled through the interphase momentum transfer function  $\mathbf{F}$  as

$$\mathbf{F} = \iiint \phi V_p \rho_p \left[ D_p (\mathbf{u}_f - \mathbf{u}_p) - \frac{1}{\rho_p} \nabla p \right] dV_p d\rho_p d\mathbf{u}_p. \quad (19)$$

### 185 3 Discretization

186 This section presents the discretization of governing equations for fracture propagation and proppant trans-  
187 port models.

#### 188 3.1 Hydraulic Fracture Propagation

189 The propagation of hydraulic fractures is governed by two fundamental equations, in which the elasticity  
190 equation is discretized by 3D DDM, and the lubrication equation is discretized using FVM.

##### 191 3.1.1 Discretized Elasticity Equation

192 The fracture domain is discretized into  $N$  uniform rectangular meshes ( $\Delta x \times \Delta y$ ). Assuming the fracture  
193 width  $w$  is piecewise constant over each element, the discretized elasticity equation is

$$p_i - \sigma_i = \sum_{j=1}^N C_{i,j} w_j. \quad (20)$$

194 Here,  $C_{i,j}$  represents the influence of the fracture width at the  $j$ th element on the normal stress at the  
195  $i$ th element and is calculated as (Crouch et al. 1983)

$$C_{i,j} = -\frac{E'}{8\pi} \left[ \frac{\sqrt{(x_i - x)^2 + (y_i - y)^2}}{(x_i - x)(y_i - y)} \right]_{x=x_j - \frac{\Delta x}{2}, y=y_j - \frac{\Delta y}{2}}^{x=x_j + \frac{\Delta x}{2}, y=y_j + \frac{\Delta y}{2}}. \quad (21)$$

##### 196 3.1.2 Discretized Lubrication Equation

197 The lubrication equation is discretized by FVM, in which the pressure and width values are stored at  
198 the center of control volumes. Here the control volumes in lubrication discretization overlap the boundary  
199 elements in the elasticity discretization. As shown in Fig.2, grid point  $P$  denotes the center of the current  
200 control volume, and grid points  $W, E, N$ , and  $S$  are the neighboring grid points of  $P$ , representing the centers

201 of the west, east, north, and south control volumes, respectively. Since the fluid flow in the fracture width  
 202 direction is negligible, we integrate Eq.3 over the elemental surface area to obtain the following expression.

$$\left( \frac{w^3 \Delta y}{\mu'} \frac{\partial p}{\partial x} \right)_e - \left( \frac{w^3 \Delta y}{\mu'} \frac{\partial p}{\partial x} \right)_w + \left( \frac{w^3 \Delta x}{\mu'} \frac{\partial p}{\partial y} \right)_n - \left( \frac{w^3 \Delta x}{\mu'} \frac{\partial p}{\partial y} \right)_s = \int_{\Delta x \times \Delta y} \left[ \frac{\partial w}{\partial t} + q_L - Q(t) \delta(\mathbf{x}) \right] dA, \quad (22)$$

203 where  $q_L = C' / \sqrt{t - \tau(\mathbf{x})}$ , representing the leak-off term. The subscripts  $e$ ,  $w$ ,  $n$ , and  $s$  denote the  
 204 control volume faces.

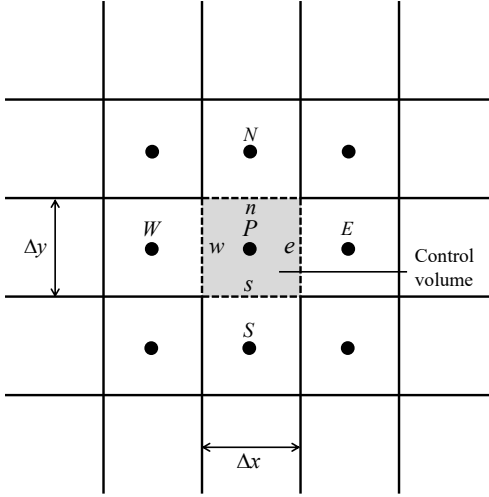


**Figure 2:** Control volumes for the grid-point cluster.  $P$  represents the current control volume, and  $W$ ,  $E$ ,  $S$ , and  $N$  denote the neighboring control volumes of  $P$  in the west, east, south, and north directions, respectively.  $w$ ,  $e$ ,  $s$ ,  $n$  are the faces between the control volumes.

205 If we evaluate the spatial and temporal derivatives from the piecewise-linear profile and use linear inter-  
 206 polation for parameters at the control volume faces, the resulting equation becomes

$$a_P p_P = a_E p_E + a_W p_W + a_N p_N + a_S p_S + b, \quad (23)$$

207 where

$$\begin{aligned} a_E &= \frac{\Delta t \Delta y}{8\mu' \Delta x} (w_P + w_E)^3, & a_W &= \frac{\Delta t \Delta y}{8\mu' \Delta x} (w_W + w_P)^3, \\ a_N &= \frac{\Delta t \Delta x}{8\mu' \Delta y} (w_P + w_N)^3, & a_S &= \frac{\Delta t \Delta x}{8\mu' \Delta y} (w_S + w_P)^3, \\ a_P &= a_E + a_W + a_N + a_S, \\ b &= (w_P^o - w_P) \Delta x \Delta y - q_L \Delta x \Delta y \Delta t + Q(t) \delta(\mathbf{x}) \Delta x \Delta y \Delta t. \end{aligned} \quad (24)$$

208 Here,  $\Delta x$  and  $\Delta y$  are the length and height of the control volume.  $\Delta t$  is the time step. A fully implicit  
 209 scheme is applied for temporal discretization. The superscript 'o' stands for the 'old' values of the parameters  
 210 at the previous time step, and the parameters without 'o' represent the 'new' values at the current time step.

### 211 3.2 Proppant Transport

212 In the proppant transport model, the fluid phase equations are discretized by FVM on an Eulerian  
 213 grid. The particle phases are solved by considering the motion of a finite number of computational parcels  
 214 representing a group of particles of identical size, velocity, and position.

#### 215 3.2.1 Discretized Fluid Phase Equations

216 A 2D staggered cartesian grid is adopted in fluid discretization to avoid the checkboard distribution of the  
 217 parameters. As shown in Fig.3, the pressure  $p$  is stored at the cell center, while the velocity components ( $u$   
 218 and  $v$ ) are stored at the face center.  $u$  and  $v$  denote the fluid velocity components in the x and y directions,  
 219 respectively. The discretized continuity equation is expressed as

$$[(\theta_f w u)_e - (\theta_f w u)_w] \Delta y + [(\theta_f w v)_n - (\theta_f w v)_s] \Delta x + \left[ \frac{\theta_f w - \theta_f^o w^o}{\Delta t} + s_l - Q(t) \delta(\mathbf{x}) \right] \Delta x \Delta y = 0, \quad (25)$$

220 where the subscripts  $e$ ,  $w$ ,  $n$ , and  $s$  denote the parameters evaluated at the center of east, west, north,  
 221 and south faces, respectively. The parameters without the face center subscripts are evaluated at the current  
 222 cell center.

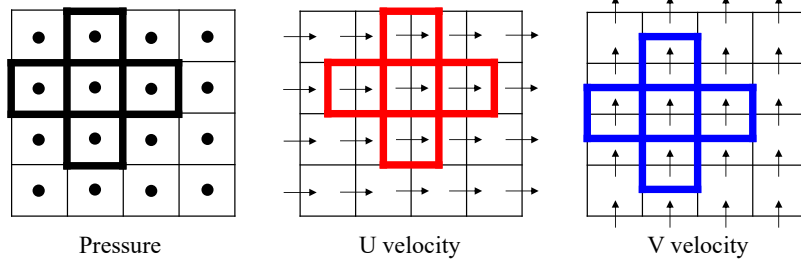


Figure 3: A 2D staggered cartesian grid for fluid discretization in proppant transport model.

223 The momentum equation of the fluid phase is discretized with respect to the  $u$  and  $v$  velocity components  
 224 as

$$\begin{cases} \frac{(\theta_f w u - \theta_f^o w^o u^o) \Delta x \Delta y}{\Delta t} + J_e^o - J_w^o + J_n^o - J_s^o = \left( \frac{1}{\rho_f} \frac{P_w - P_e}{\Delta x} - \frac{1}{\rho_f} F_x - F_{vx} \right) w \Delta x \Delta y, \\ \frac{(\theta_f w v - \theta_f^o w^o v^o) \Delta x \Delta y}{\Delta t} + J_e^o - J_w^o + J_n^o - J_s^o = \left( \frac{1}{\rho_f} \frac{P_s - P_n}{\Delta y} - \frac{1}{\rho_f} F_y - F_{wy} \right) w \Delta x \Delta y, \end{cases}, \quad (26)$$

225 where  $J_e^o$ ,  $J_w^o$ ,  $J_n^o$ , and  $J_s^o$  are the integrated total fluxes (convection plus diffusion) over the control-volume  
 226 faces, and the detailed expression of the flux terms is provided in the appendix.

227      **3.2.2 Discretized Particle Phase Equation**

228      The particle equation of motion (Eq.12) is discretized as

$$\frac{\mathbf{u}_p - \mathbf{u}_p^o}{\Delta t} = D_p (\mathbf{u}_{f,p}^o - \mathbf{u}_p) - \frac{1}{\rho_p} (\nabla p)_p - \frac{1}{\theta_p^o \rho_p} [\nabla \tau (\theta_p^o)]_p + \left(1 - \frac{\rho_f}{\rho_p}\right) \mathbf{g} + \frac{\langle \mathbf{u}_p \rangle - \mathbf{u}_p}{2\tau_D}, \quad (27)$$

229      where  $\mathbf{u}_{f,p}^o$ ,  $(\nabla p)_p$ , and  $[\nabla \tau (\theta_p^o)]_p$  are the fluid velocity, fluid pressure gradient, and particle stress  
230      gradient at particle positions, respectively.

231      **4 Solution Strategy**

232      This section introduces the numerical scheme for hydraulic fracture propagation and proppant transport,  
233      respectively. Then, a one-way coupling strategy is presented to integrate the fracture propagation and  
234      proppant transport models.

235      **4.1 Numerical Scheme for Fracture Propagation**

236      The numerical scheme for the fracture propagation process includes two parts: a solution scheme for the  
237      elasticity and lubrication equations and a fracture front-tracking approach.

238      **4.1.2 Solution Scheme for the Elasticity and Lubrication Equations**

239      The elasticity and lubrication equations (Eqs.2 and 3) are solved simultaneously by Newton-Raphson  
240      iteration at every time step. The residual form of the fully discrete coupled equations is

$$R_{rd}^i = \sum_{j=1}^N C_{i,j} w_j + \sigma_i - p_i, \quad (28)$$

$$\begin{aligned} R_{ff}^i &= \frac{\Delta y \Delta t}{8\mu' \Delta x} [(w^j)_P + (w^j)_E]^3 (p_E^i - p_P^i) + \frac{\Delta y \Delta t}{8\mu' \Delta x} [(w^j)_P + (w^j)_W]^3 (p_W^i - p_P^i) \\ &\quad + \frac{\Delta x \Delta t}{8\mu' \Delta y} [(w^j)_P + (w^j)_N]^3 (p_N^i - p_P^i) + \frac{\Delta x \Delta t}{8\mu' \Delta y} [(w^j)_P + (w^j)_S]^3 (p_S^i - p_P^i) \\ &\quad - [(w^j)_P - (w^{jo})_P] \Delta x \Delta y - \frac{C'}{\sqrt{t - \tau^i}} \Delta x \Delta y \Delta t + Q(t) \delta(\mathbf{x}_{inj}) \Delta x \Delta y \Delta t, \quad \forall i = 1, \dots, N. \end{aligned} \quad (29)$$

241      where  $R_{rd}^i$  and  $R_{ff}^i$  are the residuals for rock deformation and fluid flow at element  $i$ , respectively. The  
242      equations include two unknowns: the fracture width  $w$  and fluid pressure  $p$ . Given an approximation of  
243      the solution vector  $\mathbf{x}^{n+1,k} = [\mathbf{w}, \mathbf{p}]^{n+1,k}$ , where  $k$  and  $n+1$  denote the iteration and time levels, Newton's  
244      method leads to the following system of equations for the corrections.

$$\underbrace{\begin{bmatrix} \mathbf{J}_{rd} & \mathbf{J}_{rd \leftarrow ff} \\ \mathbf{J}_{ff \leftarrow rd} & \mathbf{J}_{ff} \end{bmatrix}}_{\mathbf{J}} \begin{bmatrix} \delta \mathbf{x}_{rd} \\ \delta \mathbf{x}_{ff} \end{bmatrix}^{n+1,k} = - \begin{bmatrix} \mathbf{R}_{rd} \\ \mathbf{R}_{ff} \end{bmatrix}^{n+1,k}, \quad (30)$$

where  $\mathbf{J}$  is the Jacobian matrix.  $\mathbf{J}_{vd}$  and  $\mathbf{J}_{ff}$  are the sub-matrices of rock deformation and fluid flow, respectively.  $\mathbf{J}_{v \leftarrow f}$  and  $\mathbf{J}_{ff \leftarrow d}$  are the coupling matrices. By solving the linearized algebraic equations (Eq. 30), we can determine the corrections  $\delta \mathbf{x}_{rd}^{n+1,k}$  and  $\delta \mathbf{x}_{ff}^{n+1,k}$  simultaneously. The approximated solution  $\mathbf{x}^{n+1,k}$  at the  $k$ th iteration then can be improved to  $\mathbf{x}^{n+1,k+1}$  as

$$\mathbf{x}^{n+1,k+1} = \mathbf{x}^{n+1,k} + \delta \mathbf{x}^{n+1,k}, \quad (31)$$

where  $\delta \mathbf{x}^{n+1,k} = [\delta \mathbf{x}_{rd}, \delta \mathbf{x}_{ff}]^{n+1,k}$ . This process is iterated to refine the estimate until the following convergence criterion is met.

$$\|\delta \mathbf{x}^{n+1,k}\|_2 < \epsilon \quad (32)$$

where  $\|\cdot\|_2$  denotes the  $l^2$  norm of the variable,  $\epsilon$  is the convergence tolerance. Given a proper initial guess, the coupled system can be solved efficiently due to the quadratic convergence of Newton's method.

#### 4.1.2 Fracture Front-Tracking Approach

The fracture propagation criterion in this study was proposed by Olson (1991, 2007).

$$\lim_{s \rightarrow 0} 0.806w \simeq \frac{K' s^{1/2}}{E'}, \quad (33)$$

where  $s$  is the inward distance from the fracture front. A constant of 0.806 was adopted to correct the fracture tip widths, addressing the overestimation by constant DDM (Olson 1991). The constant coefficient has been widely applied in previous literature for engineering purposes (Sheibani and Olson 2013; Wu and Olson 2015; Tang et al. 2016; Manchanda et al. 2020; Chen et al. 2020).

The moving fracture front is tracked by a fixed grid method (Barree 1983; Siebrits and Peirce 2002; Tang et al. 2016; Chen et al. 2020). The flexibility of the current meshing strategy is the fracture elements are only added when needed. Therefore, the model avoids storing the information of underlying Eulerian meshes, and the inactive background meshes are excluded from the solving matrices. Also, there is no need for the model to predefine the largest planar fracture footprint.

The fracture tip velocity is calculated based on the activation time of elements.

$$V_{T,i} = \frac{d_i}{t_{T,i} - t_{P,i}}, \quad (34)$$

where  $V_{T,i}$  is the fracture velocity of the tip element  $i$ .  $t_{T,i}$  is the activation time of the tip element  $i$ , and  $t_{P,i}$  is the activation time of its corresponding parent element.  $d_i$  is the distance between the centers of the tip and parent element ( $\Delta x$  in the height direction and  $\Delta y$  in the length direction).

The time step  $\Delta t$  is explicitly calculated as

$$\Delta t = \frac{\lambda \min(\Delta x, \Delta y)}{\max(V_T)} \quad (35)$$

where  $\lambda \in (0, 1)$  is a relaxation factor. A smaller  $\lambda$  corresponds to better numerical stability.

## 4.2 Numerical Scheme for Proppant Transport

The numerical scheme for proppant transport involves three parts: the interpolation functions, the numerical scheme for fluid phase equations, and the numerical scheme for particle motion.

### 4.2.1 Interpolation Functions

In proppant transport modeling, the fluid equations are discretized by FVM on the Eulerian grids, while the particles are simulated as Lagrangian points. Therefore, a bilinear interpolation function  $I(\mathbf{x}_p, \mathbf{x}_f)$  is introduced to exchange the information between the fluid and particle phases.

$$I(\mathbf{x}_p, \mathbf{x}_f) = I_x \cdot I_y, \quad (36)$$

where

$$I_x = \begin{cases} 0, & |x_p - x_f| \geq \Delta x \\ 1 - \frac{|x_p - x_f|}{\Delta x}, & |x_p - x_f| < \Delta x \end{cases}, \quad I_y = \begin{cases} 0, & |y_p - y_f| \geq \Delta y \\ 1 - \frac{|y_p - y_f|}{\Delta y}, & |y_p - y_f| < \Delta y \end{cases}. \quad (37)$$

Here,  $\mathbf{x}_p = (x_p, y_p)$  is the particle position, and  $\mathbf{x}_f = (x_f, y_f)$  is the fluid node coordinate.  $I_x$  and  $I_y$  are directional linear interpolation operators in the  $x$  and  $y$  directions, respectively. Since staggered grids (Fig. ) are adopted to avoid the checkboard pressure distribution, three sets of interpolation functions are required in two dimensions, including the cell center interpolation function  $I_{f, \text{cell}}^p(\mathbf{x}_p, \mathbf{x}_f)$ , x-face center interpolation function  $I_{f, \text{xface}}^p(\mathbf{x}_p, \mathbf{x}_f)$ , and y-face center interpolation function  $I_{f, \text{yface}}^p(\mathbf{x}_p, \mathbf{x}_f)$ . More details regarding the interpolation functions can refer to the work of Snider (2001).

With the interpolation functions, we can calculate the particle volume fraction at Eulerian cell centers  $\theta_{p,f}$  by

$$\theta_{p,f} = \frac{1}{V_f} \sum_{\kappa=1}^{N_p} n_{p\kappa} V_{p\kappa} I_{f,\text{cell}}^p(\mathbf{x}_{p\kappa}, \mathbf{x}_f), \quad (38)$$

where  $\kappa$  is the parcel index for summation.  $V_f$  is the cell volume.  $V_p$  is the particle volume.  $n_p$  is the number of particles in a parcel.  $N_p$  is the total number of parcels.

The interphase momentum transfer components at Eulerian cell face centers ( $F_{x,f}$  and  $F_{y,f}$ ) are calculated by

$$\begin{cases} F_{x,f} = \frac{1}{V_f} \sum_{\kappa=1}^{N_p} \left\{ n_{p\kappa} \rho_{p\kappa} V_{p\kappa} \left[ D_p (u_{f,p\kappa} - u_{p\kappa}) - \frac{1}{\rho_{p\kappa}} \nabla p_{x,p\kappa} \right] I_{f,x\text{face}}^p(\mathbf{x}_{p\kappa}, \mathbf{x}_f) \right\}, \\ F_{y,f} = \frac{1}{V_f} \sum_{\kappa=1}^{N_p} \left\{ n_{p\kappa} \rho_{p\kappa} V_{p\kappa} \left[ D_p (v_{f,p\kappa} - v_{p\kappa}) - \frac{1}{\rho_{p\kappa}} \nabla p_{y,p\kappa} \right] I_{f,y\text{face}}^p(\mathbf{x}_{p\kappa}, \mathbf{x}_f) \right\}. \end{cases} \quad (39)$$

Here,  $u_p$  and  $v_p$  are the particle velocity components in  $x$  and  $y$  directions, respectively.  $u_{f,p}$ ,  $v_{f,p}$ ,  $\nabla p_{x,p}$ , and  $\nabla p_{y,p}$  are the fluid velocity components and pressure gradient components interpolated at particle positions.

$$u_{f,p} = \sum_{\zeta=1}^6 u_{f\zeta} I_{f,x\text{face}}^p(\mathbf{x}_p, \mathbf{x}_{f\zeta}), \quad v_{f,p} = \sum_{\zeta=1}^6 v_{f\zeta} I_{f,y\text{face}}^p(\mathbf{x}_p, \mathbf{x}_{f\zeta}) \quad (40)$$

$$\nabla p_{x,p} = \sum_{\zeta=1}^6 \nabla p_{x\zeta} I_{f,x\text{face}}^p(\mathbf{x}_p, \mathbf{x}_{f\zeta}), \quad \nabla p_{y,p} = \sum_{\zeta=1}^6 \nabla p_{y\zeta} I_{f,y\text{face}}^p(\mathbf{x}_p, \mathbf{x}_{f\zeta}) \quad (41)$$

Here  $\zeta$  is the index for the six face center nodes bounding the particle. Note that, for the cell center interpolation function, there are nine cell center nodes bounding the particle.

#### 4.2.2 Numerical Scheme for Fluid Phase Equations

We use a modified SIMPLE (Semi-Implicit Method for Pressure-Linked Equations) to solve the fluid flow equations (Patankar 2018).

---

##### Algorithm 1 A Modified SIMPLE Algorithm

---

- 1: Initialize a guessed pressure  $p^*$ ;
  - 2: **while** ( $|p'| > \text{convergence criterion } (10^{-5})$ ) **do**
  - 3:     Solve the momentum equations (Eq.26) with an explicit scheme to obtain  $u^*$  and  $v^*$ ;
  - 4:     Solve the pressure-correction ( $p'$ );
  - 5:     Correct pressure  $p = p^* + p'$ ;
  - 6:     Correct velocity;
  - 7:     Treat the corrected  $p$  as a new guessed pressure  $p^*$ , return to step 2.
  - 8: **end while**
- 

Solving the fluid momentum equations (Eq.26) using an explicit scheme significantly improves computational efficiency. The numerical stability can be achieved once the CFL (Courant-Friedrichs-Lowy) condition (Eq. 42) is satisfied.

$$C = \Delta t \left( \frac{u}{\Delta x} + \frac{v}{\Delta y} \right) \leq C_{\max}, \quad (42)$$

301 where  $C$  is the Courant number, and  $C_{\max}$  is the maximum Courant number allowed for the system.  
 302  $C_{\max}$  less than one is applied to ensure numerical stability in the current work.

303 **4.2.3 Numerical Scheme for Particle Motion**

304 The particle velocity is computed from Eq.27 as

$$\mathbf{u}_p = \frac{\mathbf{u}_p^o + \Delta t \left\{ D_p \mathbf{u}_{f,p}^o - \frac{1}{\rho_p} (\nabla p)_p - \frac{1}{\theta_p^o \rho_p} [\nabla \tau(\theta_p^o)]_p + \left(1 - \frac{\rho_f}{\rho_p}\right) \mathbf{g} + \frac{\langle \mathbf{u}_p \rangle - \mathbf{u}_p}{2\tau_D} \right\}}{1 + \Delta t D_p}. \quad (43)$$

305 The particle position  $\mathbf{x}_p$  is then updated by

$$\mathbf{x}_p = \mathbf{x}_p^o + \Delta t \mathbf{u}_p. \quad (44)$$

306 Note that the fluid-particle drag force and particle collision damping terms in Eq.43 are treated implicitly  
 307 due to the large values of  $D_p$  and  $1/2\tau_D$ , avoiding exceedingly small time steps. Since  $D_p$  is a function of  
 308  $\mathbf{u}_p$  (Eq.13), an iterative scheme is needed in  $\mathbf{u}_p$  calculation.

309 **4.3 A One-Way Coupling Strategy for Fracture Propagation and Proppant Transport**

310 Assuming a negligible effect of proppant transport on fracture propagation, we use a one-way coupling  
 311 strategy to integrate fracture propagation and proppant transport. The numerical algorithm of the integrated  
 312 simulation is shown in Fig. 4. The fracture propagation is first solved to get the fracture geometry and fluid  
 313 leak-off rate distribution. Then, the proppant transport is simulated by solving the fully coupled fluid and  
 314 particle equations (Eqs.7, 8, and 12). In proppant transport simulation, the particle calculation has a much  
 315 smaller time step than the fluid flow calculation. Therefore, we adopt a subloop for particle calculation to  
 316 improve computational efficiency.

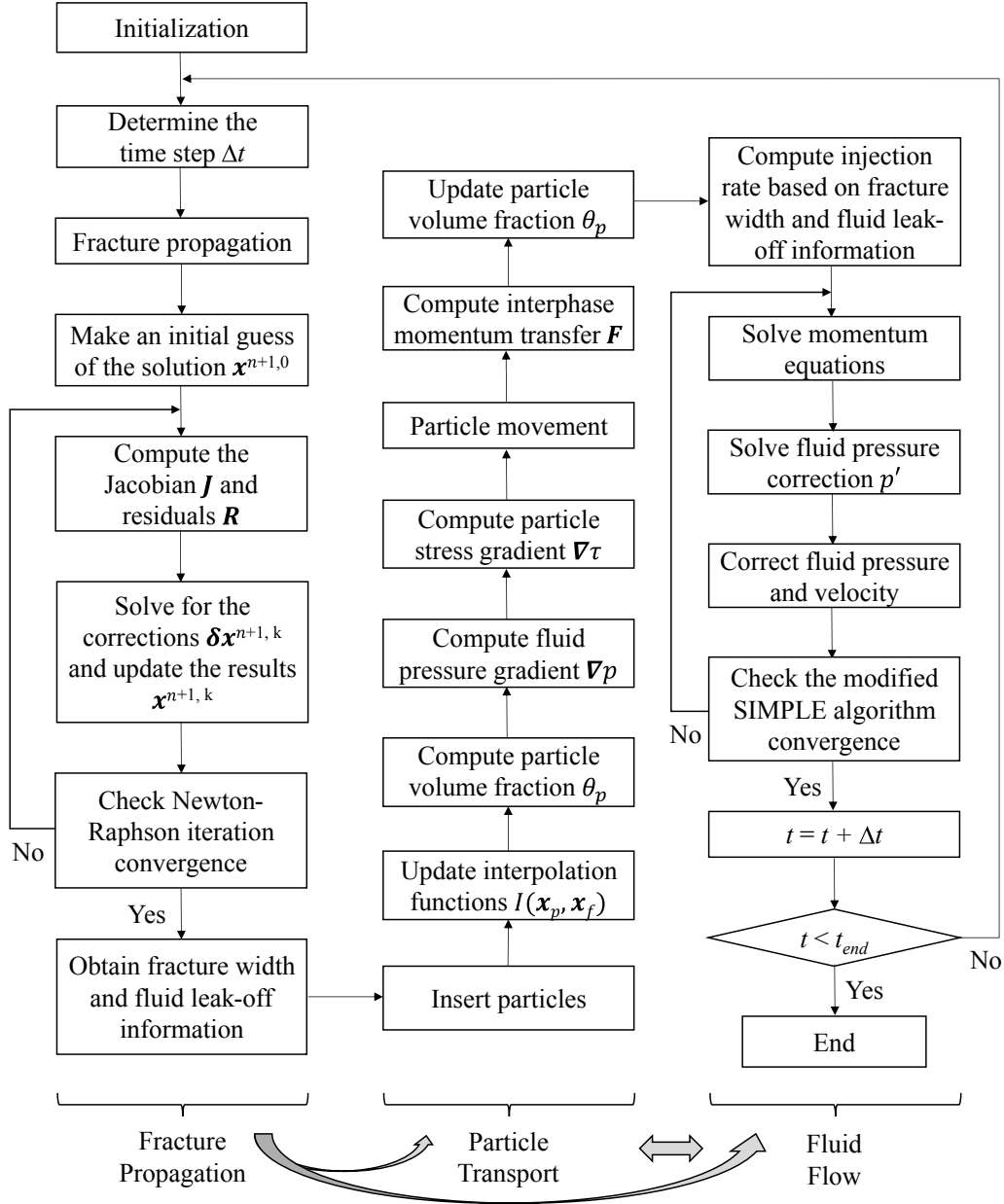


**Figure 4:** Numerical algorithm for the integrated hydraulic fracturing model. The fracture propagation and proppant transport are one-way coupled.

## 317 5 Model Validation

318 This section validates the fracture propagation and proppant transport models, respectively.

### 319 5.1 Validation for Fracture Propagation Model

320 The fracture propagation model is validated by analytical solutions of the penny-shaped (radial) fractures  
 321 and laboratory experiments for fracture propagation with stress contrast.

322      **5.1.1 Penny-Shaped Fracture Propagation**

323      The penny-shaped fracture propagation involves three physical processes, including the creation of solid  
 324      surfaces, the flow of viscous fluid, and the leak-off of fracturing fluid. The competition between these processes  
 325      leads to four limiting regimes of hydraulic fracture propagation: the storage viscosity regime ( $M$ ), leak-off  
 326      viscosity regime ( $\tilde{M}$ ), storage toughness regime ( $K$ ), and leak-off toughness regime ( $\tilde{K}$ ). Over the past two  
 327      decades, researchers have developed analytical solutions corresponding to these regimes to benchmark the  
 328      numerical results (Savitski and Detournay 2002; Bunger et al. 2005; Detournay et al. 2007; Peirce and  
 329      Detournay 2008; Dontsov 2016). As shown in Table 2, we design four cases (case I, II, III, and IV) to  
 330      validate the fracture propagation model, covering four limiting regimes.

Parameters	Case I	Case II	Case III	Case IV	Unit
Young's modulus	40	40	5	5	GPa
Poisson's ratio	0.15	0.15	0.42	0.42	/
Rock toughness	1	1	1.27	1.27	MPa.m <sup>1/2</sup>
Fluid viscosity	0.08	0.08	1.0e <sup>-3</sup>	1.0e <sup>-3</sup>	Pa.s
Injection rate	0.053	0.053	3.0e <sup>-5</sup>	3.0e <sup>-5</sup>	m <sup>3</sup> /s
Injection time	370	370	405.8	407	s
Leak-off coefficient	2.0e <sup>-7</sup>	4.0e <sup>-3</sup>	1.0e <sup>-7</sup>	4.0e <sup>-4</sup>	m/s <sup>1/2</sup>
Minimum confining stress	60	60	6	6	MPa

**Table 2:** Simulation parameters for validation cases I, II, III, and IV, representing the storage viscosity, leak-off viscosity, storage toughness, and leak-off toughness propagation regimes, respectively.

331      Solution maps are constructed to show the parametric space of each case (Figs.12 a, d, g, and j) and  
 332      validity regions of the benchmark solutions by two dimensionless parameters (Dontsov, 2016)

$$\tau = t \left( \frac{\mu'^5 E^{13} Q^3}{K'^{18}} \right)^{-1/2}, \quad (45)$$

$$\phi = \frac{\mu'^3 E^{11} C^4 Q}{K^{14}}, \quad (46)$$

333      where  $\tau$  is the dimensionless time, and  $\phi$  is the normalized leak-off. Black circle markers inside the maps  
 334      indicate the locations of the problem parameters at different times. The black arrows denote the moving  
 335      direction of the markers during the injection.

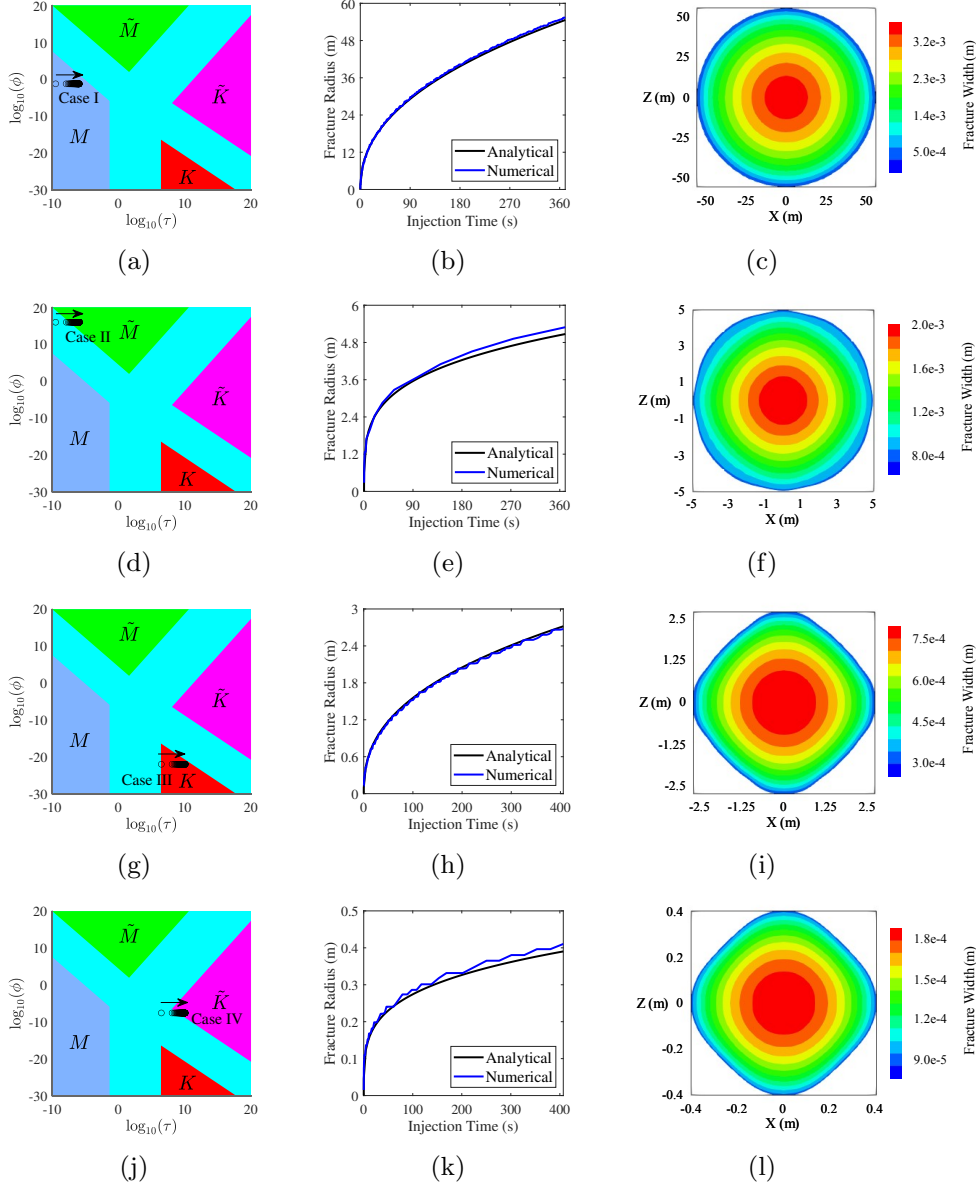


**Figure 5:** Numerical algorithm for the integrated hydraulic fracturing model. The fracture propagation and proppant transport are one-way coupled.

As shown in Figs.12 b, e, h, and k, the numerical solutions agree well with the analytical solutions for all cases in terms of the fracture radius evolution. Figs.12 c, f, i, and l show the fracture geometries of four cases at the end of the injection. Note that the fracture geometries of cases III and IV are not exactly penny-shaped because the fluid flow within the fracture becomes irrelevant in toughness-dominant cases (Donstov 2016). Previous literature reported similar results using the fixed rectangular mesh front tracking method (Zheng et al. 2019; Chen et al. 2020). Generally, the geometry deviation does not affect the results significantly, and the model can accurately simulate penny-shaped fracture propagation for engineering purposes.

343        **5.1.2 Fracture Propagation with Stress Contrast**

344        Besides the penny-shaped fracture propagation, we also apply the fracture propagation model in simu-  
 345        lating the fracture growth in a layered media with stress contrast and validate the results with laboratory  
 346        experiments (Wu et al. 2008). In a three-layer configuration, the experiment injects a viscous fluid (30 Pa.s)  
 347        into a PMMA block. The injection point is placed at the middle layer (Zone 2), with a confining stress of 7  
 348        MPa. The upper layer (Zone 1) has a higher confining stress of 11 MPa, while the lower layer (Zone 3) has  
 349        a lower confining stress of 5 MPa. The injection rate varies in time and has four stages. Other details about  
 350        the experiment can be found in Wu et al. 2008.

$$Q(t) = \begin{cases} 9 \times 10^{-4} \text{ mL/s}, & 0 < T \leq 31 \text{ s} \\ 6.5 \times 10^{-3} \text{ mL/s}, & 31 < t \leq 151 \text{ s} \\ 2.3 \times 10^{-3} \text{ mL/s}, & 151 < t \leq 701 \text{ s} \\ 0 \text{ mL/s}, & t > 701 \text{ s} \end{cases} . \quad (47)$$

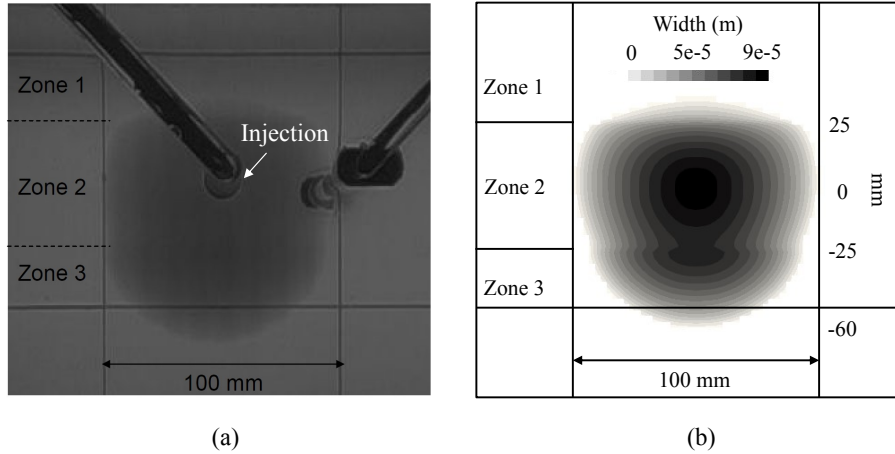


**Figure 6:** Snapshots of a growing hydraulic fracture at an injection time of 87 seconds. (a) Laboratory experimental observation (Wu et al. 2008); (b) Numerical simulation result. The confining stresses of zones 1, 2, and 3 are 11 MPa, 7 MPa, and 5 MPa, respectively. The fracture is initiated in Zone 2.

351        Fig.6 shows the snapshots of a growing hydraulic fracture at an injection time of 87 seconds. As illustrated,  
 352        the simulation achieves a similar fracture footprint to the experiment. Initiated in the middle layer (Zone  
 353        2), the fracture grows happily into the lower layer (Zone 3) due to the lower confining stress. However, the  
 354        fracture height is significantly contained in the upper zone (Zone 1) due to the higher confining stress.

355        We also compare the fracture front evolution of the simulation and experiment. The simulation agrees  
 356        well with the experiment at five different time steps (22 s, 60 s, 144 s, 376 s, and 665 s) (Fig.7). Therefore, the  
 357        current model can accurately simulate fracture propagation in a layered media with varying stress conditions.

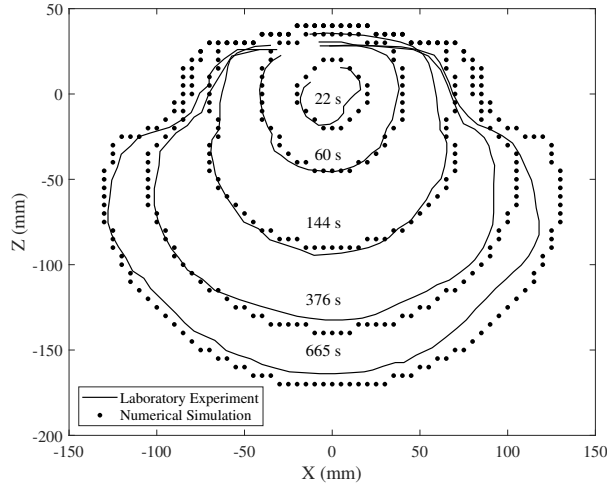


**Figure 7:** Temporal evolution of fracture front. The solid line represents the experimental observation, and the dotted data represents the numerical simulation.

## 358      5.2 Validation for Proppant Transport Model

359      We have performed two validation tests for the proppant transport model: the bimodal particle sedimen-  
 360      tation and particle transport in a vertical slot. For both tests, the numerical results are benchmarked by the  
 361      experimental results.

### 362      5.2.1 Bimodal Particle Sedimentation

363      The bimodal particle sedimentation experiment was conducted by Davis et al. 1982. The vertical  
 364      sedimentation vessel has a height of 100 cm and a square cross-section with internal dimensions of 5 cm.  
 365      The fluid is Newtonian and has a density of 992 kg/m<sup>3</sup> and a viscosity of 0.0667 N.s/m<sup>2</sup>. The experiment  
 366      used two types of particles with different densities and mean radii. The heavy particles have a density of  
 367      2990 kg/m<sup>3</sup>, a mean radius of 99  $\mu\text{m}$ , and an initial concentration of 0.01. The light particles have a density  
 368      of 2440 kg/m<sup>3</sup>, a mean radius of 68.75  $\mu\text{m}$ , and an initial concentration of 0.03. Particles are distributed  
 369      uniformly within the vessel at the beginning, and the system settles.

370      As illustrated (Figs.8a, b, and c), the heavy particles with a larger mean radius settle faster than the  
 371      light particles with a small mean radius. Two transient interfaces of the two types of particles are observed  
 372      during the settling process. We notice that the numerical and experimental results agree well (Fig.8d), thus  
 373      validating the model in simulating particle settling phenomena.

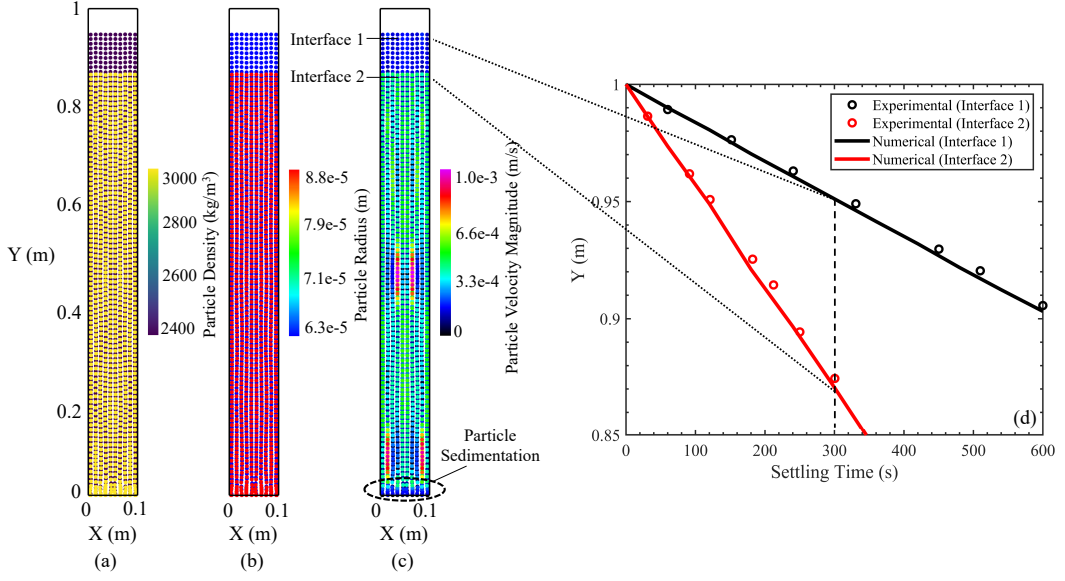


**Figure 8:** Simulation results of the bimodal particle sedimentation problem. (a), (b), and (c) show the distribution of particle density, radius, and velocity magnitude at the settling time of 300 s. (d) compares the simulation results with experimental observations (Davis et al. 1982) in terms of the height evolution of two transient interfaces.

### 374 5.2.2 Proppant Transport in a Pressure-Driven Vertical Slot

375 To mimic the proppant transport in hydraulic fractures, we validate the proppant transport model  
 376 through a laboratory experiment in which the proppant slurry is pumped into a narrow vertical slot (Chun  
 377 et al. 2020). The experimental parameters are summarized in Table 3. We use the same configuration to  
 378 conduct the numerical simulation.

Experimental Parameters	Value	Unit
Slot height	0.3048	m
Slot length	1.2192	m
Slot width	7.62e <sup>-3</sup>	m
Injection rate	3.79e <sup>-4</sup>	$\text{m}^3/\text{s}$
Fluid dynamic viscosity	1.0e <sup>-3</sup>	$\text{N} \cdot \text{s}/\text{m}^2$
Proppant density	2550	$\text{kg}/\text{m}^3$
Proppant size	30/50	mesh
Inlet proppant volume fraction	0.065845	/

**Table 3:** Experimental parameters for the proppant transport in a vertical slot.

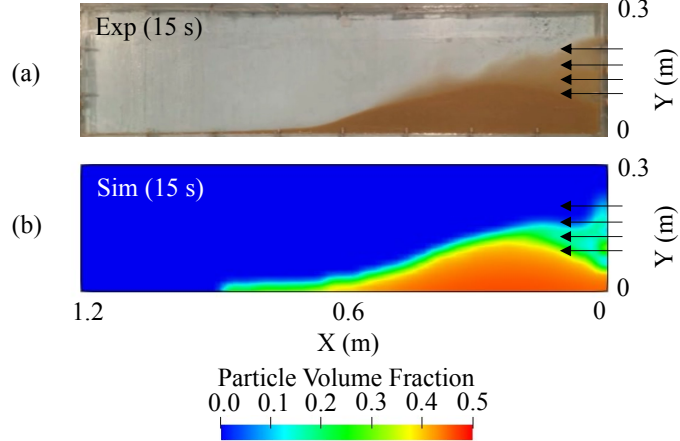


**Figure 9:** Snapshots of the proppant distribution at the injection time of 15 s. (a) represents the experimental result, and (b) corresponds to the simulation result.

Fig.9 shows the snapshots of the proppant distribution at the injection time of 15 s. As illustrated, the numerical model achieves a similar proppant bed profile to the experiment. We also compare the proppant bed profiles between the numerical simulation and laboratory experiment at three different times (5 s, 15 s, and 20 s), and the comparison shows an excellent agreement (Fig.10 ). Therefore, the P3D MP-PIC method can accurately simulate proppant transport in a narrow vertical slot.

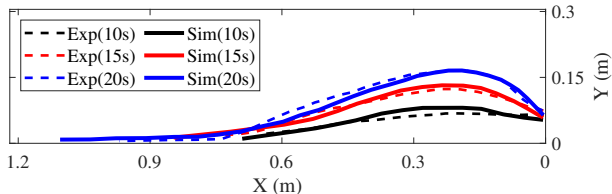


**Figure 10:** Temporal evolution of proppant bed profile. The solid lines represent the simulation results, and the dashed lines correspond to the experimental results.

## 6 Field-Scale Application

To illustrate the functionality of the current numerical approach, we apply the integrated model in simulating the hydraulic fracturing treatments in a multilayer reservoir with varying confining stresses.

### 6.1 Numerical Configuration and a Base Case

Fig.11 shows a five-layer reservoir of which layers 2, 3, and 4 are "pay zones". The perforation is in layer 3, with a higher confining stress (61.7 MPa) than in layers 2 (60 MPa) and 4 (60 MPa). Layers 1 and 5 are symmetric stress barriers. Table 4 lists the simulation parameters of the base case.

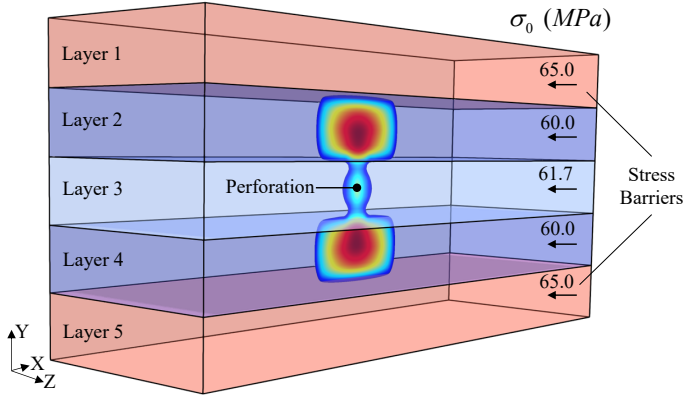


**Figure 11:** Schematics of a five-layer reservoir with varying confining stress conditions. Layers 2, 3, and 4 are pay zones, while layers 1 and 5 are stress barriers. The perforation (fracture initiation) is in layer 3. The minimum horizontal stress is perpendicular to the X-Y plane.

Parameters	Value	Unit
Young's modulus	45	GPa
Poisson ratio	0.2	/
Rock toughness	2.2	MPa · m <sup>1/2</sup>
Fluid viscosity	2	mPa.s
Leak-off coefficient	3.90e <sup>-7</sup>	m/s <sup>1/2</sup>
Injection rate	0.0265	m <sup>3</sup> /s
Total injection time	3600	s
Pad injection time	1200	s
Proppant size	40/70	mesh
Proppant density	2650	Kg/m <sup>3</sup>
Inlet proppant volume fraction	0.2	/

**Table 4:** Simulation parameters of the base case.

As shown in Table 4, the total pumping time is 1 hour, and the pad fluid injection lasts for the first 20 mins. Fig.12 presents the fracture geometry evolution during the pad injection. The left column shows the fracture width distribution (X-Y plane), and the right column illustrates the cross-sectional width profile along X=0 (Y-Z plane). Once perforated, the fracture initiates as a penny-shaped fracture in layer 3 (Fig.12a). After 30 seconds of injection, the fracture propagates symmetrically into layers 2 and 4 due to the symmetric stress condition (Fig.12b). Under the lower confining stress, the fracture grows happily in layers 2 and 4 with a large fracture length and width (Fig.12c). However, the fracture height is significantly contained by

398 layers 1 and 5 due to large stress barriers (5 MPa), resulting in an hour-glass shaped fracture footprint and  
 399 cross-sectional width profile (Fig.12d).

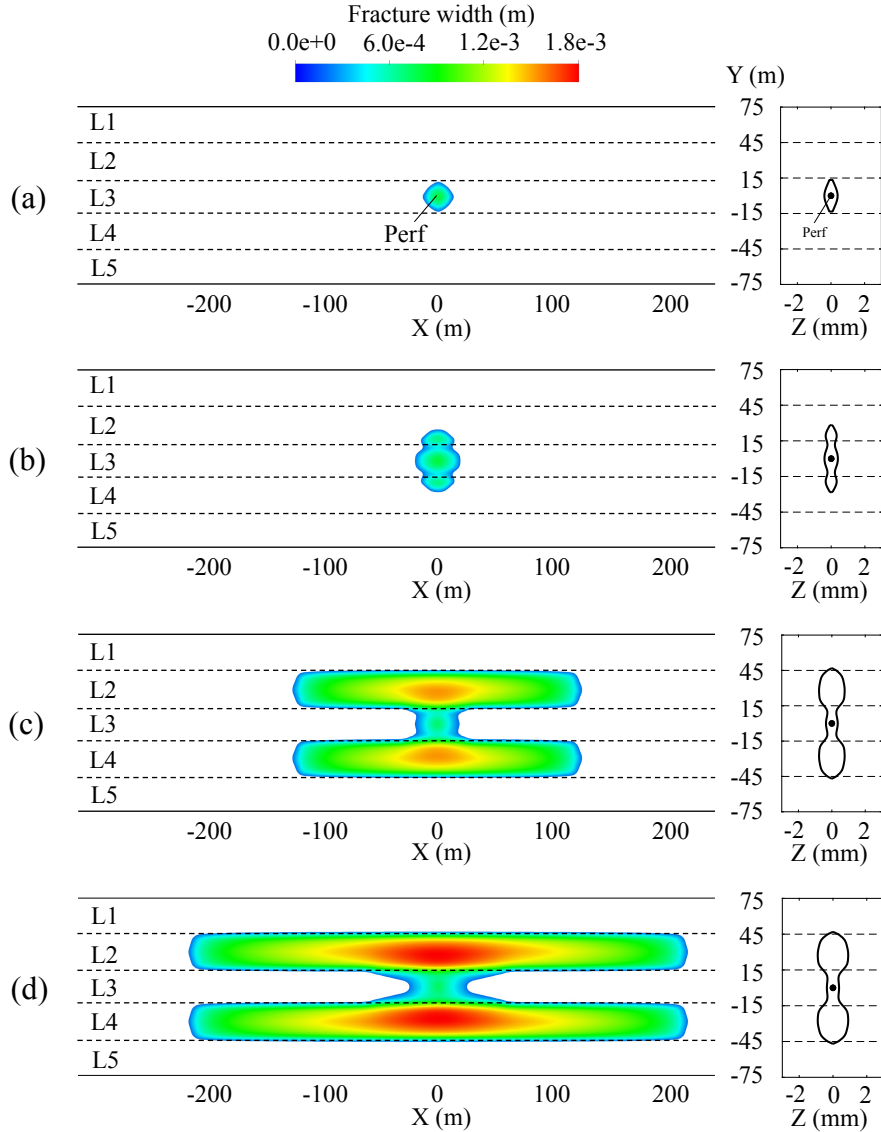


**Figure 12:** Temporal evolution of hydraulic fracture geometry during pad injection for the base case. The left column gives the fracture width distribution (X-Y plane), and the right column shows the cross-sectional width profile along  $X=0$  (Y-Z plane). (a), (b), (c), and (d) denote the results at 10 s, 30 s, 600 s, and 1200 s, respectively.

400 The proppant is loaded after the pad injection (20 mins). An annular injection zone is designed to load  
 401 particles into the fracture. Fig.13a shows the particle volume fraction distribution at 5 seconds of proppant  
 402 injection. Since all the proppant is initially suspended in the fluid, the particle volume fraction is almost  
 403 uniform, close to the inlet particle volume fraction (0.2). Due to the Lagrangian nature of the model, we  
 404 can track particle movement during the pumping process. Fig.13b shows the particle velocity magnitude

405 distribution and fracture width distribution. Fig.13c is the zoom-in view of the particle velocity magnitude  
 406 distribution. The color of particles represents the particle velocity magnitude. The arrows are the streamlines  
 407 of the particle motion, of which the angle denotes the moving direction, and the length and color indicate  
 408 the particle velocity magnitude.

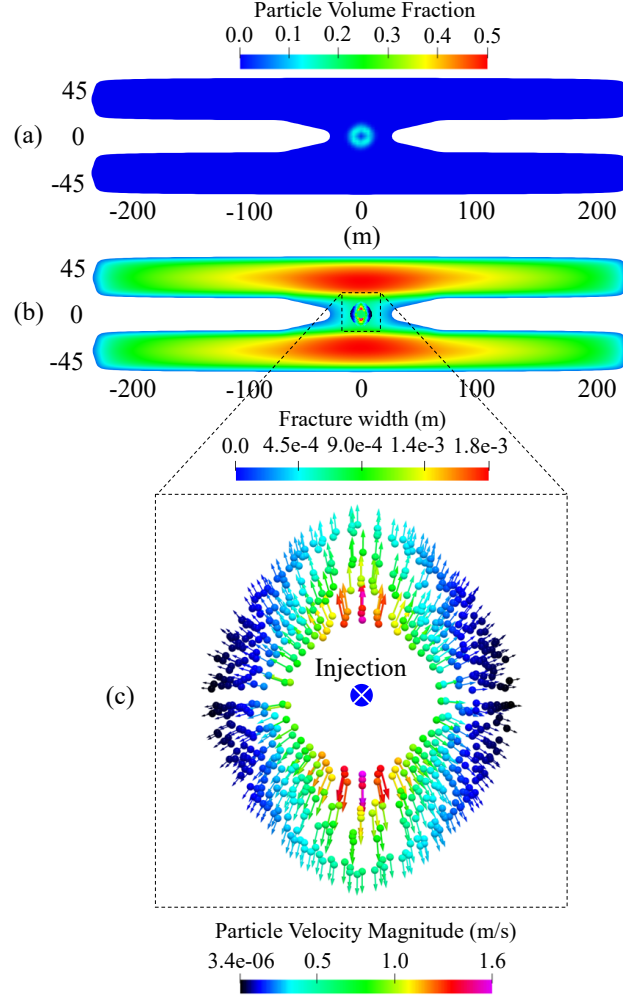


**Figure 13:** Simulation results of the base case at an initial stage of proppant injection (1205 s). (a) Particle volume fraction distribution; (b) Particle velocity magnitude distribution and fracture width distribution; (c) Zoom-in view of particle velocity magnitude distribution.

409 As illustrated, the proppant achieves the highest velocity near the injection point. The particle velocity  
 410 gradually decreases after injection. Also, it is observed that the particles move faster vertically than laterally.  
 411 The reasons for the particle velocity difference are two folds. Firstly, most fracturing fluid rushes into layers 2  
 412 and 4 due to the lower confining stress. The dominant fluid flow leads to the preferential proppant transport  
 413 in the vertical direction via the fluid-particle drag. Secondly, the small fracture width in layer 3 results in  
 414 large wall friction from the fracture surface, thus inhibiting the lateral fluid and particle transport.

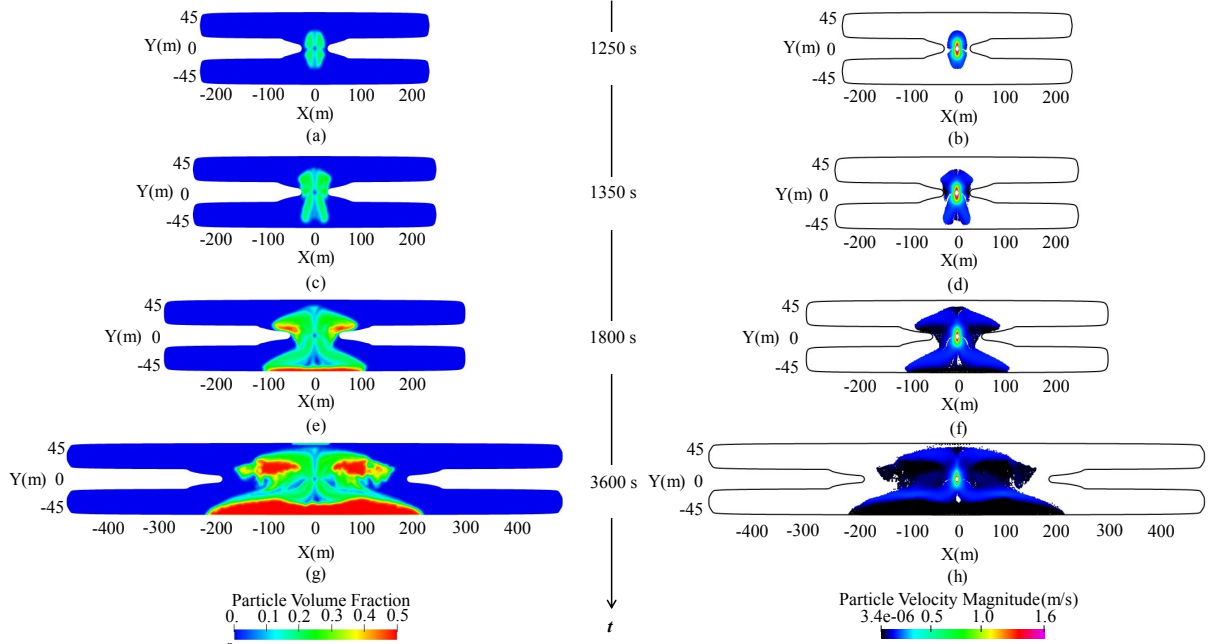


**Figure 14:** Temporal evolution of particle volume fraction distribution (a, c, e, and g) and particle velocity magnitude (b, d, f, and h) distribution for base case.

Fig.14 shows the temporal evolution of particle volume fraction and particle velocity magnitude distribution. Initially, all the particles are suspended and go with the fracturing fluid (Figs.14 a and b). Due to the gravity effect, the particles moving downward have a higher particle velocity and transport for a longer distance into layer 4 (Figs.14 c and d). As the injection continues, the proppant gradually settles at the fracture bottom as the proppant bed (Figs.14 e and f). Note that the proppant also accumulates on the top of layer 3. This is because layer 3 has a small fracture width under the high confining stress, which hinders the proppant from falling and causes the proppant bridging effect. The proppant bed and bridging effect become more significant at the end of the injection (Figs.14 g and h). By comparing the particle volume fraction distribution with the particle velocity magnitude distribution, we notice that the suspended particles have a much higher particle velocity than the packed particles. The proppant accumulation always corresponds to a low particle velocity region. Besides, we find that even though the hydraulic fracture propagates long distances and achieves a large fracture area, the proppant coverage area is limited. Most proppant settles near the injection point, leaving a large portion of the fracture unproped.

## 6.2 Effect of Proppant Size

To improve the proppant delivery in fracturing treatments, we investigate the impact of proppant size on the proppant transport by designing two other cases with proppant sizes of 30/50 and 100 meshes. Except for the proppant size, all the other parameters are the same as the base case.

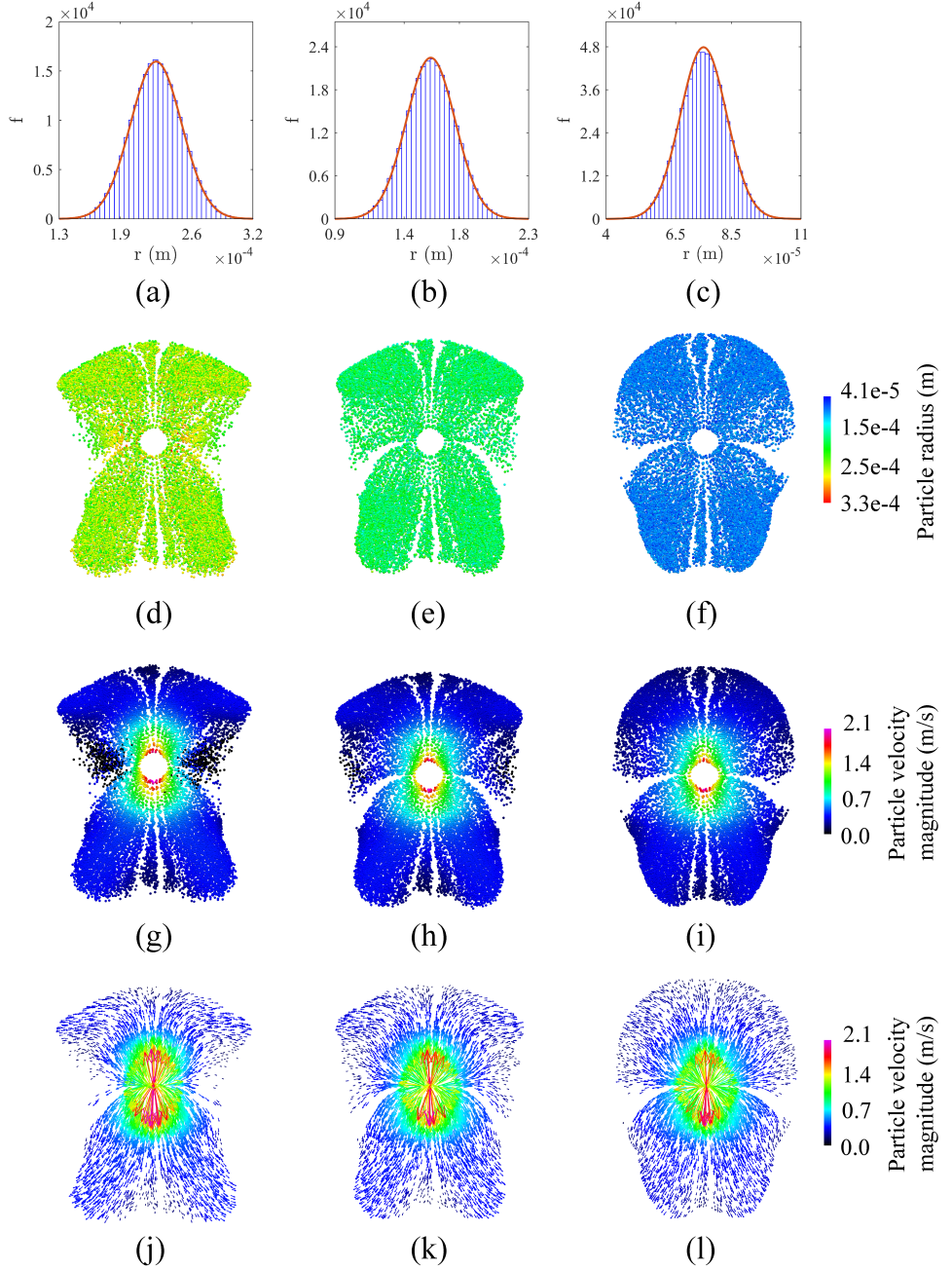


**Figure 15:** Simulation results of particles at the injection time of 1320 s for three cases. From left to right, three columns of figures represent the results of 30/50-, 40/70-, and 100-mesh cases. (a), (b), and (c) show the normal distribution of particle radius. (d), (e), and (f) display the spatial distribution of particle radius. (g), (h), and (i) present the particle velocity magnitude distribution. (j), (k), and (l) denote the streamlines of the particle movement.

As illustrated in Figs.15a, b, and c, we assign a Gaussian/normal proppant size distribution to each case. Multi-size particles (within a specified range) are randomly loaded into the fracture at every timestep to mimic the realistic field proppant injection process. Figs.15d, e, and f show the spatial distribution of

435 particle radius for all cases after injecting for 1320 s. Even though most proppant is suspended in the fluid  
 436 at early proppant injection, particle size can noticeably impact the proppant placement. As the particle size  
 437 decreases from 30/50 mesh to 100 mesh, the proppant becomes more uniformly distributed and transports  
 438 further upwards. Figs.15g, h, and i present the particle velocity magnitude distribution. For all the cases,  
 439 the proppant achieves the highest velocity near the injection point and moves faster vertically than laterally.  
 440 In the 30/50-mesh case, the lateral proppant transport is strongly inhibited in layer 3. This is because the  
 441 proppant diameter is close to the fracture width. Therefore, the fracture can trap large particles and cause  
 442 the bridging effect. The trapped particles can be significantly reduced with a smaller proppant size. The  
 443 particle streamlines in Figs.15 j, k, and l also provide similar information on particle movement.

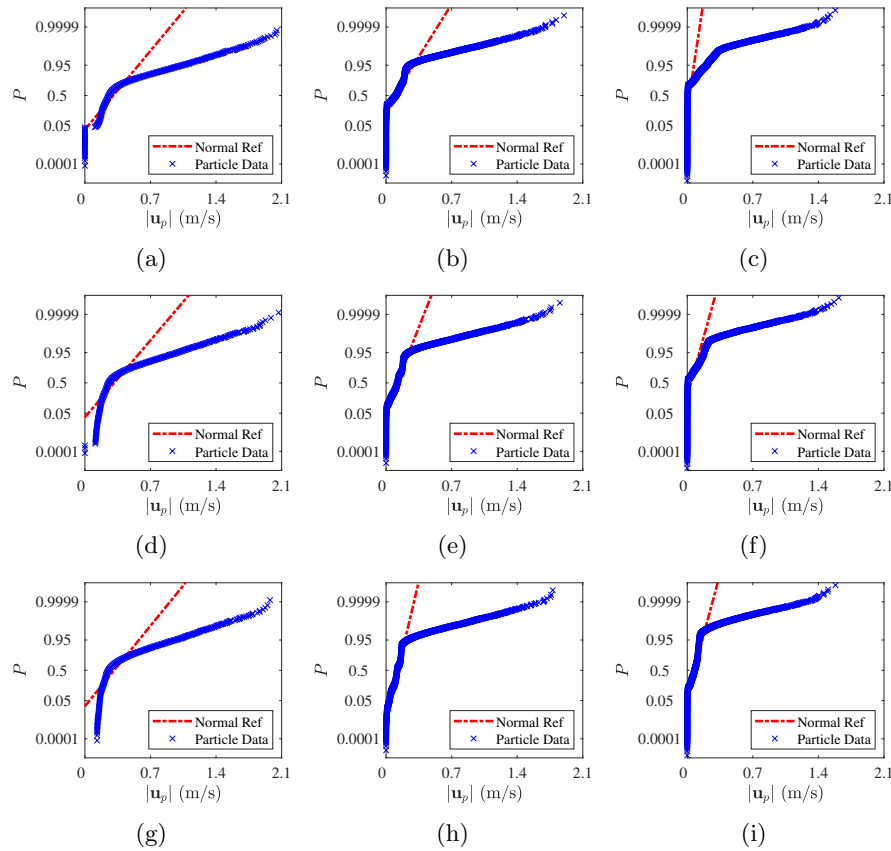


**Figure 16:** Probability plots for particle velocity magnitude distribution at different injection times for three cases. From left to right, three columns of figures represent the results of 1260 s, 1800 s, and 3600 s of injection, respectively.

444 For detailed quantitative analyses of particle transport, we track the particle velocity magnitude ( $|u_p|$ )  
 445 distribution during the pumping process using probability plots (Fig.16). The probability plots show the  
 446  $|u_p|$  of each parcel and the corresponding cumulative probability. The blue marker represents the simulation  
 447 results of  $|u_p|$ , and the red dashed line denotes the normal distribution reference. From the probability plots,

448 we have two findings. Firstly, the percent of packed proppant increases during the pumping process for all  
 449 cases. From 1260 s to 3600 s of injection, the probability of small  $|\mathbf{u}_p| (\approx 0)$  gradually increases, indicating  
 450 more particles are accumulated as the proppant pack. Secondly, the larger proppant is easier to form the  
 451 proppant pack. In 30/50- and 40/70-mesh cases, the proppant pack occurs early (Figs.16a and d) because  
 452 large particles are trapped by the small fracture width in layer 3. As the proppant size decreases to 100  
 453 mesh, there is no packed proppant at the initial proppant injection (Fig.16g). Except for the initial proppant  
 454 pack, the final cumulative probability of packed proppant also drops significantly from about 0.71 to 0.18  
 455 when the proppant size decreases from 30/50 mesh to 100 mesh (Figs. 16c, f, and i).

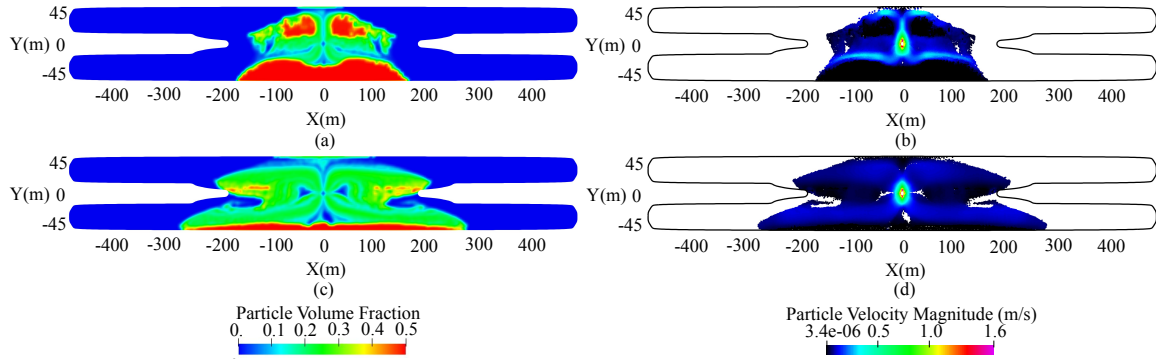


**Figure 17:** Final distribution of particle volume fraction and particle velocity magnitude for 30/50- and 100-mesh cases.

456 Fig.17 presents the final (3600 s) distribution of particle volume fraction and particle velocity magnitude  
 457 for 30/50- and 100-mesh cases. As illustrated, proppant size can significantly impact the proppant placement  
 458 in the hydraulic fracture. The 30/50-mesh case has a severe proppant settling, so most proppant is accu-  
 459 mulated as the proppant bed near the injection point. In contrast, for the 100-mesh case, a large amount  
 460 of proppant is suspended in the fluid, and the proppant settling phenomenon has been strongly mitigated.  
 461 Therefore, the 100-mesh proppant can transport for a longer distance and achieve a larger propped area  
 462 (proppant coverage area).

463 To better evaluate the proppant distribution, we calculate the temporal evolution of the total fracture  
 464 area and propped area during the pumping process. As shown in Fig.18, the total fracture area increases  
 465 from the beginning of the injection. After 20 minutes of pad fluid injection, we start loading the proppant  
 466 into the fracture. Then, the propped area gradually increases. Generally, the propped area is much smaller  
 467 than the total fracture area. The final propped area of the 30/50-mesh case is only about 30.9% of the  
 468 total fracture area, which means a large portion of the created hydraulic fracture is ineffective. A smaller  
 469 proppant size can significantly improve the propped area by mitigating the particle settling. As illustrated,  
 470 the final propped area of the 100-mesh case is 59.3% higher than the 30/50-mesh case.

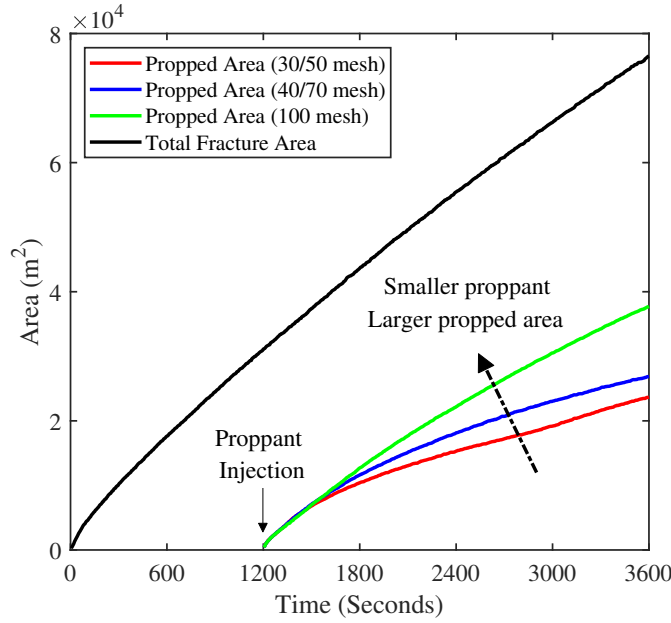


**Figure 18:** Temporal evolution of total hydraulic fracture area and propped area for three cases. The first 1200 s is pad fluid injection, after which the proppant is loaded into the fracture.

## 471 7 Conclusions

472 This paper develops an integrated hydraulic fracturing simulator by coupling a PL3D fracture propagation  
 473 model with an E-L proppant transport model. In the fracture propagation model, the fluid flow and rock  
 474 deformation are solved by FVM and DDM, respectively. The proppant transport is modeled by an efficient  
 475 P3D MP-PIC method. The fracture propagation and proppant transport models are one-way coupled to  
 476 consider the effect of dynamic fracture geometries and fluid leak-off on the proppant transport. Compared  
 477 to existing models, the current model has three advantages: 1. This model can simulate complex fracture  
 478 propagation and proppant transport behaviors in multilayer reservoirs with varying stress conditions; 2.  
 479 Due to its Lagrangian nature, the model can easily deal with multi-modal particle simulations and avoid the  
 480 problem of numerical diffusion; 3. The model is computationally efficient for conducting industrial field-scale  
 481 simulations.

482 After the model development, we apply the model to simulate the fracturing treatment in a five-layer  
 483 reservoir. The results show that the complex fracture geometry in the multilayer reservoir can significantly  
 484 affect the proppant transport. Due to a large fracture width, the low-stress layers become preferential flow  
 485 paths for the fluid and particles. However, in high-stress layers, the proppant can be easily trapped by  
 486 the fracture because the fracture width is close to the particle diameter. Besides the fracture geometry,  
 487 proppant size also significantly impacts the proppant placement. Smaller proppant has a less severe settling

and bridging, thus achieving a much larger propped area during the pumping process. The field-scale application demonstrates that the current model can simulate the fracturing treatments at the industrial field scale. The results can be used to design and optimize hydraulic fracturing operations.

## Appendix

### Derivation of Flux Terms

$J_e^o, J_w^o, J_n^o$ , and  $J_s^o$  are the integrated total fluxes over the east, west, north, and south face of the control volume, respectively. As shown in Fig.3 , this work has two fluid velocity components  $u$  and  $v$ . Each velocity component has its own set of control volumes due to the staggered grids. Therefore, there are two sets of fluxes corresponding to the control volume of  $u$  and  $v$ . Here, we first derive the fluxes for the  $u$  velocity component.

The momentum equation of  $u$  velocity component is

$$\frac{1}{w} \frac{\partial (\theta_f w u)}{\partial t} + \frac{1}{w} \nabla \cdot (w \theta_f \mathbf{u}_f u - w \mu_f \nabla u) = -\frac{1}{\rho_f} \nabla p - \frac{1}{\rho_f} F_x - F_{wx}. \quad (48)$$

Then, we denote  $\mathbf{J} = w \theta_f \mathbf{u}_f u - w \mu_f \nabla u$  and integrate the equation over the  $u$  velocity control volume to obtain the following equation.

$$\frac{(\theta_f w u - \theta_f^o w^o u^o)_P \Delta x \Delta y}{\Delta t} + J_e^o - J_w^o + J_n^o - J_s^o = \left( \frac{1}{\rho_f} \frac{P_w - P_e}{\Delta x} - \frac{1}{\rho_f} F_{xP} - F_{wxP} \right) w_P \Delta x \Delta y, \quad (49)$$

where

$$J_e^o = (w \theta u^o)_e \Delta y u_e^o - \frac{w_e \mu_f \Delta y}{\rho_f \delta_x} \left( \frac{\partial u^o}{\partial (x/\delta_x)} \right)_e, \quad (50)$$

$$J_w^o = (w \theta u^o)_w \Delta y u_w^o - \frac{w_w \mu_f \Delta y}{\rho_f \delta_x} \left( \frac{\partial u^o}{\partial (x/\delta_x)} \right)_w, \quad (51)$$

$$J_n^o = (w \theta v^o)_n \Delta x u_n^o - \frac{w_n \mu_f \Delta x}{\rho_f \delta_y} \left( \frac{\partial u^o}{\partial (y/\delta_y)} \right)_n, \quad (52)$$

$$J_s^o = (w \theta v^o)_s \Delta x u_s^o - \frac{w_s \mu_f \Delta x}{\rho_f \delta_y} \left( \frac{\partial u^o}{\partial (y/\delta_y)} \right)_s. \quad (53)$$

502 Here  $\delta_x$  and  $\delta_y$  are the diffusion lengths in the x and y directions. In this study,  $\delta_x$  equals  $\Delta x$ , and  $\delta_y$   
 503 equals  $\Delta y$ . With an explicit practice, the flux terms are denoted by the superscript 'o' and regarded as 'old'  
 504 values. For convenience,  $J_e^o$ ,  $J_w^o$ ,  $J_n^o$ , and  $J_s^o$  can also be written as

$$J_e^o = F_e^o u_e^o - D_e^o \left( \frac{\partial u^o}{\partial(x/\delta_x)} \right)_e, \quad (54)$$

$$J_w^o = F_w^o u_w^o - D_w^o \left( \frac{\partial u^o}{\partial(x/\delta_x)} \right)_w, \quad (55)$$

$$J_n^o = F_n^o u_n^o - D_n^o \left( \frac{\partial u^o}{\partial(y/\delta_y)} \right)_n, \quad (56)$$

$$J_s^o = F_s^o u_s^o - D_s^o \left( \frac{\partial u^o}{\partial(y/\delta_y)} \right)_s, \quad (57)$$

505 where  $F$  indicates the strength of the convection, while  $D$  is the diffusion conductance. To construct  
 506 a general framework into which various numerical schemes can be fitted, we represent the fluxes as the  
 507 following forms by dividing  $D$  from two sides of the flux expressions.

$$J_e^{o*} = \frac{J_e^o}{D_e^o} = P_e^o u_e^o - \left( \frac{\partial u^o}{\partial(x/\delta_x)} \right)_e, \quad (58)$$

$$J_w^{o*} = \frac{J_w^o}{D_w^o} = P_w^o u_w^o - \left( \frac{\partial u^o}{\partial(x/\delta_x)} \right)_w, \quad (59)$$

$$J_n^{o*} = \frac{J_n^o}{D_n^o} = P_n^o u_n^o - \left( \frac{\partial u^o}{\partial(y/\delta_y)} \right)_n, \quad (60)$$

$$J_s^{o*} = \frac{J_s^o}{D_s^o} = P_s^o u_s^o - \left( \frac{\partial u^o}{\partial(y/\delta_y)} \right)_s, \quad (61)$$

508 where  $P = F/D$  is the Peclet number. By evaluating the value of  $u$  and the gradient  $\partial u / \partial(x/\delta_x)$ ,  
 509  $\partial u / \partial(y/\delta_y)$  at the interface by the value of  $u$  at control volume center, we can obtain the following expression  
 510 of the fluxes.

$$J_e^0 = \{ D_e^0 A (|P_e^0|) + [F_e^0, 0] \} u_P^o - \{ D_e^0 A (|P_e^0|) + [-F_e^0, 0] \} u_E^o, \quad (62)$$

$$J_w^o = \{D_w^o A(|P_w^o|) + \llbracket F_w^o, 0 \rrbracket\} u_W^o - \{D_w^o A(|P_w^o|) + \llbracket -F_w^o, 0 \rrbracket\} u_P^o, \quad (63)$$

$$J_n^o = \{D_n^o A(|P_n^o|) + \llbracket F_n^o, 0 \rrbracket\} u_P^o - \{D_n^o A(|P_n^o|) + \llbracket -F_n^o, 0 \rrbracket\} u_N^o, \quad (64)$$

$$J_s^o = \{D_s^o A(|P_s^o|) + \llbracket F_s^o, 0 \rrbracket\} u_S^o - \{D_s^o A(|P_s^o|) + \llbracket -F_s^o, 0 \rrbracket\} u_P^o \quad (65)$$

511 In this way, various numerical schemes can be easily incorporated into the discretization equation by  
 512 different choices of the function  $A(|P|)$ . This study adopts the power law scheme, in which  $A(|P|) =$   
 513  $\llbracket 0, (1 - 0.1|P|)^5 \rrbracket$ . Here, we define  $\llbracket , \rrbracket$  to denote the greater of two values. The flux terms of  $v$  velocity  
 514 component can be derived easily similar to the  $u$  velocity component.

## 515 Declaration of Competing Interest

516 The authors declare that they have no competing interests.

## 517 References

- 518 Adachi, J., Siebrits, E. M., Peirce, A., and Desroches, J. 2007. Computer simulation of hydraulic fractures.  
 519 *International Journal of Rock Mechanics and Mining Sciences*, 44(5), 739-757.
- 520 Andrews, M. J., and O'Rourke, P. J. 1996. The multiphase particle-in-cell (MP-PIC) method for dense  
 521 particulate flows. *International Journal of Multiphase Flow*, 22(2), 379-402.
- 522 Baldini, M., Carlevaro, C. M., Pugnaloni, L. A., and Sánchez, M. 2018. Numerical simulation of proppant  
 523 transport in a planar fracture. A study of perforation placement and injection strategy. *International Journal*  
 524 *of Multiphase Flow*, 109, 207-218.
- 525 Barree, R. D. 1983. A practical numerical simulator for three-dimensional fracture propagation in heteroge-  
 526 neous media. *SPE reservoir simulation symposium*. OnePetro.
- 527 Barree, R.D., and M.W. Conway. "Experimental and Numerical Modeling of Convective Proppant Trans-  
 528 port." *SPE Annual Technical Conference and Exhibition*, New Orleans, Louisiana, September 1994.
- 529 Boronin, S. A., and Osipov, A. A. 2014. Effects of particle migration on suspension flow in a hydraulic  
 530 fracture. *Fluid Dynamics*, 49(2), 208-221.
- 531 Bunger, A. P., Detournay, E., and Garagash, D. I. 2005. Toughness-dominated hydraulic fracture with  
 532 leak-off. *International Journal of Fracture*, 134(2), 175-190.

- 533 Bunger, A. P., and Cruden, A. R. 2011. Modeling the growth of laccoliths and large mafic sills: Role of  
534 magma body forces. *Journal of Geophysical Research: Solid Earth*, 116(B2).
- 535 Carter, E.D. 1957. Optimum fluid characteristics for fracture extension. In: Drilling and Production Prac-  
536 tices. (edited by Howard, G.C. and Fast, C.R.), *American Petroleum Institute*, Tulsa OK, pp.261–270.
- 537 Chen, M., Guo, T., Zou, Y., Zhang, S., and Qu, Z. 2022. Numerical Simulation of Proppant Transport Cou-  
538 pled with Multi-Planar-3D Hydraulic Fracture Propagation for Multi-Cluster Fracturing. *Rock Mechanics*  
539 and *Rock Engineering*, 55(2), 565-590.
- 540 Chen, M., Zhang, S., Li, S., Ma, X., Zhang, X., and Zou, Y. 2020. An explicit algorithm for modeling planar  
541 3D hydraulic fracture growth based on a super-time-stepping method. *International Journal of Solids and*  
542 *Structures*, 191, 370-389.
- 543 Chun, T., Li, Y., and Wu, K. 2020. Comprehensive experimental study of proppant transport in an inclined  
544 fracture. *Journal of Petroleum Science and Engineering*, 184, 106523.
- 545 Crouch, S. L., Starfield, A. M., and Rizzo, F. J. 1983. Boundary element methods in solid mechanics.
- 546 Crowe, C. T., Schwarzkopf, J. D., Sommerfeld, M., and Tsuji, Y. 2011. *Multiphase Flows with Droplets and*  
547 *Particles*.
- 548 Detournay, E. 2004. Propagation regimes of fluid-driven fractures in impermeable rocks. *International*  
549 *Journal of Geomechanics*, 4(1), 35-45.
- 550 Detournay, E., Peirce, A. P., and Bunger, A. P. 2007. Viscosity-dominated hydraulic fractures. *1st Canada-*  
551 *US rock mechanics symposium*. OnePetro.
- 552 Detournay, E. 2016. Mechanics of hydraulic fractures. *Annual review of fluid mechanics*, 48, 311-339.
- 553 Detournay, E., Cheng, A. D., Roegiers, J. C., and McLennan, J. D. 1989. Poroelasticity considerations in  
554 in-situ stress determination by hydraulic fracturing. In *International Journal of Rock Mechanics and Mining*  
555 Sciences and Geomechanics Abstracts (Vol. 26, No. 6, pp. 507-513). Pergamon.
- 556 Dontsov, E. V., and Peirce, A. P. 2014. Slurry flow, gravitational settling and a proppant transport model  
557 for hydraulic fractures. *Journal of Fluid Mechanics*, 760, 567-590.
- 558 Dontsov, E. V., Peirce, A. P. 2015. Proppant transport in hydraulic fracturing: crack tip screen-out in  
559 KGD and P3D models. *International Journal of Solids and Structures*, 63, 206-218.
- 560 Dontsov, E. V. 2016. An approximate solution for a penny-shaped hydraulic fracture that accounts for  
561 fracture toughness, fluid viscosity and leak-off. *Royal Society open science*, 3(12), 160737.
- 562 Dontsov, E., and Suarez-Rivera, R. 2021. Representation of high-resolution rock properties on a coarser grid  
563 for hydraulic fracture modeling. *Journal of Petroleum Science and Engineering*, 198, 108144.
- 564 Economides, M. J., and Nolte, K. G. 1989. Reservoir stimulation (Vol. 2, pp. 6-10). Englewood Cliffs, NJ:  
565 Prentice Hall.

- 566 Frank, U., and Barkley, N. 1995. Remediation of low permeability subsurface formations by fracturing  
567 enhancement of soil vapor extraction. *Journal of hazardous materials*, 40(2), 191-201.
- 568 Garagash, D., and Detournay, E. 2000. The tip region of a fluid-driven fracture in an elastic medium. *J.  
569 Appl. Mech.*, 67(1), 183-192.
- 570 Geertsma, J., and De Klerk, F. 1969. A rapid method of predicting width and extent of hydraulically induced  
571 fractures. *Journal of petroleum technology*, 21(12), 1571-1581.
- 572 Ghassemi, A. 2012. A review of some rock mechanics issues in geothermal reservoir development. *Geotech-  
573 nical and Geological Engineering*, 30(3), 647-664.
- 574 Gidaspow, D. 1994. Multiphase flow and fluidization: continuum and kinetic theory descriptions. *Academic  
575 press*.
- 576 Gu, M., and Mohanty, K. K. 2014. Effect of foam quality on effectiveness of hydraulic fracturing in shales.  
577 *International Journal of Rock Mechanics and Mining Sciences*, 70, 273-285.
- 578 Harris, S. E., and Crighton, D. G. 1994. Solitons, solitary waves, and voidage disturbances in gas-fluidized  
579 beds. *Journal of Fluid Mechanics*, 266, 243-276.
- 580 Hills, D. A., Kelly, P. A., Dai, D. N., and Korsunsky, A. M. 2013. Solution of crack problems: the distributed  
581 dislocation technique (Vol. 44). *Springer Science and Business Media*.
- 582 Hu, X., Wu, K., Li, G., Tang, J., and Shen, Z. 2018. Effect of proppant addition schedule on the proppant  
583 distribution in a straight fracture for slickwater treatment. *Journal of Petroleum Science and Engineering*,  
584 167, 110-119.
- 585 Huang, J., Hao, Y., Settgast, R. R., White, J. A., Mateen, K., and Gross, H. 2022. Validation and Appli-  
586 cation of a Three-Dimensional Model for Simulating Proppant Transport and Fracture Conductivity. *Rock  
587 Mechanics and Rock Engineering*, 1-23.
- 588 Jeffrey, R. G., Chen, Z., Mills, K. W., and Pegg, S. 2013. Monitoring and measuring hydraulic fracturing  
589 growth during preconditioning of a roof rock over a coal longwall panel. *ISRM International Conference for  
590 Effective and Sustainable Hydraulic Fracturing*. OnePetro.
- 591 Kim, H., Xie, L., Min, K. B., Bae, S., and Stephansson, O. 2017. Integrated in situ stress estimation by  
592 hydraulic fracturing, borehole observations and numerical analysis at the EXP-1 borehole in Pohang, Korea.  
593 *Rock Mechanics and Rock Engineering*, 50(12), 3141-3155.
- 594 Kou, R., Moridis, G. J., and Blasingame, T. A. 2018. Analysis and modeling of proppant transport in  
595 inclined hydraulic fractures. *SPE Hydraulic Fracturing Technology Conference and Exhibition*. OnePetro.
- 596 Kou, R., Moridis, G., and Blasingame, T. 2019. Bridging criteria and distribution correlation for prop-  
597 pant transport in primary and secondary fracture. *SPE Hydraulic Fracturing Technology Conference and  
598 Exhibition*. OnePetro.

- 599 Khristianovic SA, Zheltov YP. 1955. Formation of vertical fractures by means of highly viscous fluids. Proc.  
600 4th World Petrol. Congr., Rome, Vol. II, pp. 579–86. London: World Petroleum Council
- 601 Kumar, D., Liu, B., and Ghassemi, A. 2021. Numerical Simulation of Proppant Transport and Deposition  
602 in Complex Hydraulic-Natural Fracture Networks. *SPE/AAPG/SEG Unconventional Resources Technology*  
603 *Conference*. OnePetro.
- 604 Lecampion, B., and Desroches, J. 2015. Simultaneous initiation and growth of multiple radial hydraulic  
605 fractures from a horizontal wellbore. *Journal of the Mechanics and Physics of Solids*, 82, 235-258.
- 606 Li, S., and Zhang, D. 2021. Development of 3-D Curved Fracture Swarms in Shale Rock Driven by  
607 Rapid Fluid Pressure Buildup: Insights from Numerical Modeling. *Geophysical Research Letters*, 48(8),  
608 e2021GL092638.
- 609 Luo, B., Wong, G. K., and Han, Y. 2023. Modeling of dynamic bridging of solid particles in multiple  
610 propagating fractures. *International Journal of Solids and Structures*, 262, 112078.
- 611 Manchanda, R., Zheng, S., Hirose, S., and Sharma, M. M. 2020. Integrating reservoir geomechanics with  
612 multiple fracture propagation and proppant placement. *SPE Journal*, 25(02), 662-691.
- 613 Mao, S., Zhang, Z., Chun, T., and Wu, K. 2021. Field-scale numerical investigation of proppant transport  
614 among multicluster hydraulic fractures. *SPE Journal*, 26(01), 307-323.
- 615 Mao, S., Siddhamshetty, P., Zhang, Z., Yu, W., Chun, T., Kwon, J. S. I., and Wu, K. 2021. Impact of  
616 proppant pumping schedule on well production for slickwater fracturing. *SPE Journal*, 26(01), 342-358.
- 617 Mao, S., Zeng, J., Wu, K., and Zhang, D. 2022. Lagrangian Numerical Simulation of Proppant Transport  
618 in Channel Fracturing. *SPE Journal*, 26(01), 342-358. doi: <https://doi.org/10.2118/212828-PA>
- 619 McClure, M. W., and Horne, R. N. 2014. An investigation of stimulation mechanisms in Enhanced Geother-  
620 mal Systems. *International Journal of Rock Mechanics and Mining Sciences*, 72, 242-260.
- 621 Mendelsohn, D. A. 1984. A review of hydraulic fracture modeling—part I: general concepts, 2D models,  
622 motivation for 3D modeling. *ASME J. Energy Res. Technol*
- 623 Mobbs, A. T., and Hammond, P. S. 2001. Computer simulations of proppant transport in a hydraulic  
624 fracture. *SPE Production and Facilities*, 16(02), 112-121.
- 625 Munson, B. R., Young, D. F., Okiishi, T. H., and Huebsch, W. W. 2006. *Fundamentals of Fluid Mechanics*,  
626 John Wiley and Sons. Inc., USA.
- 627 Murdoch, L. C. 2002. Mechanical analysis of idealized shallow hydraulic fracture. *Journal of Geotechnical  
628 and Geoenvironmental Engineering*, 128(6), 488-495.
- 629 Nordgren, R. P. 1972. Propagation of a vertical hydraulic fracture. *SPE Journal*, 12(04), 306-314.
- 630 Olson, J. E. 1991. Fracture mechanics analysis of joints and veins. *Stanford University*.
- 631 Olson, J. E. 2007. Fracture aperture, length and pattern geometry development under biaxial loading: a

- 632 numerical study with applications to natural, cross-jointed systems. *Geological Society*, London, Special  
633 Publications, 289(1), 123-142.
- 634 O'Rourke, P. J., and Snider, D. M. 2010. An improved collision damping time for MP-PIC calculations of  
635 dense particle flows with applications to polydisperse sedimenting beds and colliding particle jets. *Chemical  
636 Engineering Science*, 65(22), 6014-6028.
- 637 Patankar, S. V. 2018. Numerical heat transfer and fluid flow. *CRC press*.
- 638 Patankar, N. A., and Joseph, D. D. 2001. Lagrangian numerical simulation of particulate flows. *International  
639 Journal of Multiphase Flow*, 27(10), 1685-1706.
- 640 Peirce, A., and Detournay, E. 2008. An implicit level set method for modeling hydraulically driven fractures.  
641 *Computer Methods in Applied Mechanics and Engineering*, 197(33-40), 2858-2885.
- 642 Perkins, T. K., and Kern, L. R. 1961. Widths of hydraulic fractures. *Journal of petroleum technology*, 13(09),  
643 937-949.
- 644 Poła, J., Bancewicz, M., and Koza, Z. 2017. Is Magnus effect relevant for proppant settling in narrow  
645 fractures?. *Energy Procedia*, 125, 443-449.
- 646 Pollard, D. D., and Holzhausen, G. 1979. On the mechanical interaction between a fluid-filled fracture and  
647 the Earth's surface. *Tectonophysics*, 53(1-2), 27-57.
- 648 Roostaei, M., Nouri, A., Fattahpour, V., and Chan, D. 2018. Numerical simulation of proppant transport  
649 in hydraulic fractures. *Journal of Petroleum Science and Engineering*, 163, 119-138.
- 650 Roper, S. M., and Lister, J. R. 2005. Buoyancy-driven crack propagation from an over-pressured source.  
651 *Journal of Fluid Mechanics*, 536, 79-98.
- 652 Roper, S. M., and Lister, J. R. 2007. Buoyancy-driven crack propagation: the limit of large fracture  
653 toughness. *Journal of Fluid Mechanics*, 580, 359-380.
- 654 Salimzadeh, S., Zimmerman, R. W., and Khalili, N. 2020. Gravity hydraulic fracturing: A method to create  
655 self-driven fractures. *Geophysical Research Letters*, 47(20), e2020GL087563.
- 656 Savitski, A. A., and Detournay, E. 2002. Propagation of a penny-shaped fluid-driven fracture in an imper-  
657 meable rock: asymptotic solutions. *International Journal of Solids and Structures*, 39(26), 6311-6337.
- 658 Sharma, M. M. and Gadde, P. B. 2005. The Impact of Proppant Retardation on Propped Fracture  
659 Lengths. *SPE Annual Technical Conference and Exhibition*, Dallas, Texas, USA, 9–12 October. SPE-97106-  
660 MS.
- 661 Shiozawa, S., and McClure, M. 2016. Simulation of proppant transport with gravitational settling and  
662 fracture closure in a three-dimensional hydraulic fracturing simulator. *Journal of Petroleum Science and  
663 Engineering*, 138, 298-314.
- 664 Siddhamshetty, P., Mao, S., Wu, K., and Kwon, J. S. I. 2020. Multi-size proppant pumping schedule of hy-

- 665 hydraulic fracturing: Application to a MP-PIC model of unconventional reservoir for enhanced gas production.  
666 *Processes*, 8(5), 570.
- 667 Siebrits, E., and Peirce, A. P. 2002. An efficient multilayer planar 3D fracture growth algorithm using a  
668 fixed mesh approach. *International Journal for Numerical Methods in Engineering*, 53(3), 691-717.
- 669 Snider, D. M. 2001. An incompressible three-dimensional multiphase particle-in-cell model for dense particle  
670 flows. *Journal of computational physics*, 170(2), 523-549.
- 671 Spence, D. A., Sharp, P. W., and Turcotte, D. L. 1987. Buoyancy-driven crack propagation: a mechanism  
672 for magma migration. *Journal of Fluid Mechanics*, 174, 135-153.
- 673 Suri, Y., Islam, S. Z., and Hossain, M. 2020. Proppant transport in dynamically propagating hydraulic  
674 fractures using CFD-XFEM approach. *International journal of rock mechanics and mining sciences*, 131,  
675 104356.
- 676 Tang, H., Winterfeld, P. H., Wu, Y. S., Huang, Z. Q., Di, Y., Pan, Z., and Zhang, J. 2016. Integrated  
677 simulation of multi-stage hydraulic fracturing in unconventional reservoirs. *Journal of Natural Gas Science  
678 and Engineering*, 36, 875-892.
- 679 Tang, J., and Wu, K. 2018. A 3-D model for simulation of weak interface slippage for fracture height  
680 containment in shale reservoirs. *International Journal of Solids and Structures*, 144, 248-264.
- 681 Tong, S., and Mohanty, K. K. 2016. Proppant transport study in fractures with intersections. *Fuel*, 181,  
682 463-477.
- 683 Tsai, V. C., and Rice, J. R. 2010. A model for turbulent hydraulic fracture and application to crack  
684 propagation at glacier beds. *Journal of Geophysical Research: Earth Surface*, 115(F3).
- 685 Tsuo, Y. P., and Gidaspow, D. 1990. Computation of flow patterns in circulating fluidized beds. *AIChE  
686 Journal*, 36(6), 885-896.
- 687 van As, A., and Jeffrey, R. G. 2002. Hydraulic fracture growth in naturally fractured rock: mine through  
688 mapping and analysis. In Proceedings of the 5th North American Rock Mech. Symposium and the 17th  
689 Tunneling Association of Canada Conference (NARMSTAC conference) (pp. 7-10).
- 690 Wen, H., Yang, R., Huang, Z., Zheng, Y., Wu, X., and Hu, X. 2020. Numerical simulation of proppant  
691 transport in liquid nitrogen fracturing. *Journal of Natural Gas Science and Engineering*, 84, 103657.
- 692 Wen, C. Y. 1966. Mechanics of fluidization. In Fluid Particle Technology, *Chem. Eng. Progress*. Symposium  
693 Series (Vol. 62, pp. 100-111).
- 694 Weng, X., Kresse, O., Cohen, C., Wu, R.,and Gu, H. 2011. Modeling of hydraulic-fracture-network propa-  
695 gation in a naturally fractured formation. *SPE Production and Operations*, 26(04), 368-380.
- 696 Wu, C. H., and Sharma, M. M. 2019. Modeling proppant transport through perforations in a horizontal  
697 wellbore. *SPE Journal*, 24(04), 1777-1789.

- 698 Wu, K., and Olson, J. E. 2015. Simultaneous multifracture treatments: fully coupled fluid flow and fracture  
699 mechanics for horizontal wells. *SPE Journal*, 20(02), 337-346.
- 700 Wu, R., Bunger, A. P., Jeffrey, R. G., and Siebrits, E. 2008. A comparison of numerical and experimental  
701 results of hydraulic fracture growth into a zone of lower confining stress. *The 42nd US rock mechanics*  
702 *symposium*. OnePetro.
- 703 Xu, H., Rutqvist, J., and Birkholzer, J. 2020. A study of thermal pressurization and potential for hydro-  
704 fracturing associated with nuclear waste disposal in argillaceous claystone. *International Journal of Rock*  
705 *Mechanics and Mining Sciences*, 136, 104536.
- 706 Zeng, J., Li, H., and Zhang, D. 2016. Numerical simulation of proppant transport in hydraulic fracture with  
707 the upscaling CFD-DEM method. *Journal of Natural Gas Science and Engineering*, 33, 264-277.
- 708 Zeng, J., Li, H., and Zhang, D. 2019. Numerical simulation of proppant transport in propagating fractures  
709 with the multiphase particle-in-cell method. *Fuel*, 245, 316-335.
- 710 Zeng, J., Li, H., and Zhang, D. 2021. Direct numerical simulation of proppant transport in hydraulic  
711 fractures with the immersed boundary method and multi-sphere modeling. *Applied Mathematical Modelling*,  
712 91, 590-613.
- 713 Zeng, J., Li, H., Li, S., and Zhang, D. 2022. Evaluating the Transport Performance of Novel-Shaped Proppant  
714 in Slickwater Fracturing with the Multiscale Modeling Framework. *SPE Journal*, 1-16.
- 715 Zhang, B., Gamage, R. P., Zhang, C., and Wanniarachchi, A. 2022. Hydrocarbon recovery: Optimized  
716 CFD-DEM modeling of proppant transport in rough rock fractures. *Fuel*, 311, 122560.
- 717 Zhang, X., Yang, L., Weng, D., Wang, Z., and Jeffrey, R. G. 2022. Numerical Study on Proppant Transport  
718 in Hydraulic Fractures Using a Pseudo-3D Model for Multilayered Reservoirs. *SPE Journal*, 27(01), 77-92.
- 719 Zhang, Z., Mao, S., Shang, Z., Chun, T., and Wu, K. 2020. Numerical Study of Proppant Transport  
720 in Field-Scale Fractures for Slickwater Fracturing. *54th U.S. Rock Mechanics/Geomechanics Symposium*.  
721 OnePetro.
- 722 Zhang, Z., Mao, S., Zhao, H., and Wu, K. 2020. Simulation of proppant transport in field-scale curved  
723 fractures. *SPE/AAPG/SEG Unconventional Resources Technology Conference*. OnePetro.
- 724 Zheng, S., Manchanda, R., Shrivastava, K., and Sharma, M. M. 2019. Linearized Predictor Method for  
725 the Efficient Iterative Solution of Coupled Geomechanics–Fracture Flow Problems. *53rd U.S. Rock Mechan-*  
726 *ics/Geomechanics Symposium*. OnePetro.
- 727 Zimmermann, G., Blöcher, G., Reinicke, A., and Brandt, W. 2011. Rock specific hydraulic fracturing and  
728 matrix acidizing to enhance a geothermal system—concepts and field results. *Tectonophysics*, 503(1-2),  
729 146-154.
- 730 Zoback, M. D., and Haimson, B. C. 1982. Status of the hydraulic fracturing method for in-situ stress

<sup>731</sup> measurements. *23rd U.S. Symposium on Rock Mechanics (USRMS)*. OnePetro.